

1 **Revision 2**

2

3 **Hydrothermal monazite trumps rutile: applying U-Pb**
4 **geochronology to evaluate complex mineralization ages of**
5 **the Katbasu Au-Cu deposit, Western Tianshan, Northwest**
6 **China**

7

8 Jiahao Zheng^{1,2*}, Ping Shen², Wanyi Feng³

9 ¹ Department of Earth and Space Sciences, Southern University of Science and
10 Technology, Shenzhen 518055, China

11 ² Key Laboratory of Mineral Resources, Institute of Geology and Geophysics,
12 Chinese Academy of Sciences, Beijing 100029, China

13 ³ Department of Ocean Science and Engineering, Southern University of Science and
14 Technology, Shenzhen 518055, China

15

16

17 *Corresponding author: Dr. Jiahao Zheng

18 Email address: joey-zen@163.com

19 Southern University of Science and Technology, 1088 Xueyuan Avenue, Shenzhen
20 518055, China

21 Phone: +86 0755-88018862; fax: +86 0755-88015519.

22

23

Abstract

24 The Tianshan orogenic belt hosts several world-class gold deposits and is one of
25 the largest gold provinces on Earth. The Katbasu Au-Cu deposit in the Chinese
26 Western Tianshan is hosted in a granite intrusion. Previous researchers have shown
27 that the main gold ores formed much later than the ore-hosting granite. However, the
28 formation age of Cu mineralization and its possible link to Au mineralization remain
29 poorly understood. This paper reports detailed mineralogical studies, combined with
30 zircon U-Pb, in situ hydrothermal monazite as well as rutile U-Pb ages to constrain
31 the timing of Cu mineralization and its possible link to Au mineralization. The two
32 main ore types in the Katbasu deposit include Cu-Au ores with pyrite-chalcopyrite
33 veins, which crosscut the granite, and Au ores with massive pyrite and quartz as the
34 main minerals. The Cu-Au ores are spatially associated with diorite that intruded the
35 granite, and they are overprinted by massive gold ores. Detailed mineralogical studies
36 show that chalcopyrite is the main Cu-bearing mineral in the Cu-Au ores, and it is
37 closely associated with some native gold, monazite, and rutile.

38 Secondary ion mass spectrometer (SIMS) U-Pb dating of zircon grains from the
39 ore-hosting granite and mafic enclave yielded concordant ages of 354.1 ± 1.6 Ma and
40 355.8 ± 1.7 Ma, respectively. The diorite that intruded the granite has a zircon U-Pb
41 age of 352.0 ± 3.2 Ma. The trace element compositions of the monazite suggest they
42 were formed by hydrothermal fluids rather than inherited from the ore-hosting granite.
43 Hydrothermal monazite coexisting with chalcopyrite and native gold yielded a
44 concordant age of 348.7 ± 2.3 Ma, and the W-rich hydrothermal rutile grains

45 associated with the chalcopyrite yielded a U-Pb age of 345 ± 27 Ma, indicating an
46 early Cu-Au mineralization event prior to the major Au mineralization (ca. 323-311
47 Ma). The formation time of early Cu-Au mineralization is consistent with the
48 emplacement age of the diorite and may be of magmatic-hydrothermal origin,
49 whereas the main Au has no genetic associations with magmatic rocks in the ore
50 district and may belong to the orogenic type. Monazite geochronology provided a
51 more reliable age constraint than rutile in the Katbasu Au-Cu deposit, and we suggest
52 hydrothermal monazite has advantages over rutile in dating the mineralization ages of
53 gold deposits.

54

55 **Keywords:** Hydrothermal monazite; Rutile; Geochronology; Katbasu Au-Cu deposit;
56 Western Tianshan

57

58 **1. Introduction**

59 The formation ages of ore deposits are critical for understanding their genesis
60 and making exploration strategies. Among various types of ore deposit, it is
61 notoriously difficult to determine the age of gold deposits due to a lack of suitable
62 dating minerals (e.g., Stein 2014; Zheng et al. 2020). The most commonly used dating
63 methods in gold deposits include sericite $^{40}\text{Ar}/^{39}\text{Ar}$ ages (Goldfarb et al. 1991; Mao et
64 al. 2004; Li et al. 2012), arsenopyrite and pyrite Re-Os ages (Kirk et al. 2002; Morelli
65 et al. 2007; Le Mignot et al. 2017), and to a lesser extent molybdenite Re-Os ages

66 (Selby et al. 2002; Zhai et al. 2019). Dating the gold mineralization ages using the
67 abovementioned methods can be challenging due to (1) sericite with low closure
68 temperatures may yield mixed ages induced by multiple hydrothermal events
69 (Chiaradia et al. 2013), (2) extremely low Re and Os contents in many arsenopyrite
70 and pyrite grains make it difficult to produce a reliable isochron age (Stein et al. 2000),
71 and (3) molybdenite is rare in most gold deposits. In addition to pyrite, arsenopyrite,
72 and sericite, hydrothermal monazite and rutile have been observed in many gold
73 deposits, and their U-Th-Pb ages have also been used to constrain the timing of gold
74 mineralization (Jemielita et al. 1990; Rasmussen et al. 2006; Cabral et al. 2013;
75 Fielding et al., 2017; Deng et al. 2020). However, there has been little attempt to
76 evaluate the relative accuracy and suitability between hydrothermal monazite and
77 rutile in gold deposits.

78 Located in the southern part of the Central Asian Orogenic Belt (CAOB), the
79 Tianshan belt (also known as Tien Shan) stretches for more than 2000 km across
80 Uzbekistan and Kyrgyzstan to Xinjiang in China. It hosts several world-class gold
81 deposits (e.g., Muruntau with 6137 t Au, Frimmel 2008; Almalyk with 2000 t Au,
82 Cooke et al. 2005; and Kumtor with 1100 t Au, Mao et al. 2004), and is one of the
83 largest Phanerozoic gold provinces on Earth. The Chinese Western Tianshan orogenic
84 belt in Xinjiang hosts many Paleozoic gold deposits and occurrences, several of which
85 contain ore reserves more than 50 tons (e.g., Sawayaerdun orogenic gold deposit with
86 130 t Au, Liu et al. 2002; Axi and Jingxi-Yelmand epithermal gold deposits with 70 t
87 and 95 t Au, White 2007), and it is one of the most important gold ore belts in China

88 (Zhu et al. 2016). Previous researchers have documented the geological characteristics,
89 nature of the ore fluids, ore-forming ages, stable and radioactive isotopes, as well as
90 geodynamic settings of these gold deposits (e.g., Long et al. 2005; Chiaradia et al.
91 2006; Liu et al. 2007; Zhai et al. 2009; Zhu 2011; Chen et al. 2012; Zheng et al. 2016;
92 An and Zhu 2018).

93 The Katbasu deposit is a newly discovered Au-Cu deposit in the Chinese
94 Western Tianshan with a gold reserve of 87 t at an average grade of 3.84 g/t, and
95 copper reserves of 50,000 tons (Yang et al. 2013; Xing et al. 2018). Since 2008,
96 regional geological field mapping and chemical sampling at Katbasu led to the
97 identification of an alteration and mineralization zone. Subsequent geological and
98 geophysical surveys, followed by drilling programs during 2011 to 2012, confirmed
99 the discovery of a large Au-Cu deposit hosted in the granite (Yang et al. 2013).
100 Recent researchers have elaborated on the chronology and genesis of ore-hosting
101 granites, ore deposit geology, structural characteristics, gold mineralization ages, fluid
102 inclusions, and H-O-S-Pb isotopes of the Katbasu gold-copper deposit (Feng et al.
103 2014; Gao et al. 2015; Zhang et al. 2015; Dong et al. 2018; Liu et al. 2018; Zhao et al.
104 2019). The diachronous ages of pyrite in the Katbasu deposit (310.9 ± 4.2 Ma from
105 pyrite Re-Os, Zhang et al. 2015; 322.5 ± 6.8 Ma from pyrite Rb-Sr, Dong et al.
106 2018) indicate that the gold mineralization occurred much later than the ore-hosting
107 granite (zircon U-Pb ages of 359.8 -345.5 Ma, Feng et al. 2014; Dong et al. 2018; Li
108 et al. 2018). However, the timing of copper mineralization and its potential links with
109 gold mineralization in the Katbasu deposit is not clear, and its genesis remains

110 controversial. Our recent study on the Katbasu Au-Cu deposit found that in addition
111 to a large amount of pyrite and quartz, the Au-Cu ores also contain many
112 hydrothermal monazite and rutile grains. Detailed mineralogical studies have shown
113 that these hydrothermal monazite and rutile grains are closely related to chalcopyrite
114 and native gold. These findings make the Katbasu deposit an ideal object for studying
115 the relative accuracy and suitability of monazite and rutile chronology in
116 hydrothermal gold deposits.

117 In this contribution, we use geological observation and detailed mineralogy,
118 together with zircon, hydrothermal monazite, and rutile chronology in the Katbasu
119 Au-Cu deposit, with aims to (1) study the Cu mineralization age of the Katbasu gold
120 deposit and its potential links to the Au mineralization; (2) discuss the genetic type of
121 the Katbasu deposit; and (3) evaluate the relative accuracy and suitability between
122 hydrothermal monazite and rutile for geochronology in gold deposits.

123 **2. Regional geology**

124 The Chinese Western Tianshan, situated in the southern part of the Central Asian
125 Orogenic Belt (CAOB; Fig. 1a), is herein defined as all parts of the mountain range in
126 China located west of the Urumqi-Korla Road, and bounded by the southern margin
127 of the Junggar Basin and the northern margin of Tarim Basin (Fig. 1b). It was formed
128 by the amalgamations of the Tarim, Yili, and Junggar blocks (Gao et al. 1998; Zhu et
129 al. 2009). It can be further divided into the North Tianshan Accretionary Complex
130 (NTAC), the Yili-Central Tianshan, and the South Tianshan Orogenic Belt (STOB)

131 from north to south.

132 The NTAC is mainly composed of Devonian to Early Carboniferous volcanic
133 and sedimentary rocks, and ophiolitic slices (Feng and Zhu 2018). It was formed by
134 southward subduction of North Tianshan ocean beneath Yili-Central Tianshan along
135 the North Tianshan suture zone. The Yili-Central Tianshan contains a Precambrian
136 basement and overlying Paleozoic volcanic-sedimentary strata. Voluminous granitoid
137 plutons intruded into the Ordovician-Early Carboniferous volcanic-sedimentary strata
138 (Feng and Zhu 2019). The STOB mainly consists of Lower Cambrian-Carboniferous
139 sedimentary rocks and interlayered volcanic rocks, high/ultrahigh pressure
140 metamorphic rocks, ophiolitic components, and Permian granitoids (Gao et al. 2009).

141 The Katbasu Au deposit is located in the southern part of the Yili-Central
142 Tianshan terrane, adjacent to the northern part of the STOB (Fig. 1b). The South
143 Tianshan oceanic slab subducted northwards beneath the Yili-Central Tianshan in the
144 Early Silurian, producing the continental arc magmatism. The subduction probably
145 terminated in the Late Carboniferous, and subsequent orogenesis occurred between
146 Late Carboniferous and Early Permian (Feng and Zhu 2019). The NEE trending North
147 Nalati fault and the South Nalati fault are the two major regional faults in this area,
148 and some E-W and NEE striking faults occur as secondary structures (Fig. 2a). The
149 strata that crop out north of the North Nalati fault are mainly Carboniferous
150 volcanic-sedimentary rocks. The main intrusive rocks in the region are Carboniferous
151 granitoids, as well as some Silurian, Devonian, and Permian granitoids.

152

153 **3. Deposit geology and mineralization**

154 The Katbasu deposit contains gold reserve of about 87 t and copper reserves of
155 50,000 tons (Xing et al., 2018). In the Katbasu mining area, the volcano-sedimentary
156 succession is mainly composed of Silurian tuff and limestone (Fig. 2b). Some
157 unmineralized garnet-epidote skarn occurs locally at the boundary between granitoids
158 and limestone. Several NEE-trending faults in the mining area, and the main gold
159 orebodies are located in the granite between F5 and F6 faults. The igneous rocks in
160 the Katbasu Au deposit consist mainly of granite, granodiorite, and diorite (Figs. 2b
161 and c). The granite is a homogeneous pluton emplaced in a single phase. Some mafic
162 enclaves occur in the granite, and they have diffuse contacts with the hosting granite
163 (Fig. 3b). The mafic enclaves typically have rounded shapes, but may be subangular.
164 The mafic enclaves have relatively homogenous mineral sizes and textures from their
165 rims to cores, indicating that they crystallized almost coevally with the hosting granite.
166 The granite (Fig. 3a) consists of potassium feldspar, plagioclase, quartz, and minor
167 biotite, whereas the mafic enclaves are composed mainly of plagioclase and biotite.
168 Some diorite dikes intruded the granite pluton, and they generally have sharp contacts
169 with the hosting granite as some Cu-Au mineralization occurs at their contact zones
170 (Xing et al. 2016). The diorites are composed mainly of plagioclase and amphibole
171 with some disseminated pyrite and chalcopyrite (Figs. 3c and 4a).

172 The orebodies are spatially associated with the Early Carboniferous granite. The
173 main Au orebodies are distributed between the F5 and F6 faults and nearly parallel to
174 them. Ore-hosting granite in the Katbasu deposit include various types of potassic,

175 chlorite, and sulfide-quartz vein alterations. Orebodies of the Katbasu Au deposit are
176 usually lens-shaped and hosted in the granite (Figs. 2b and c). The ore-hosting granite
177 has been dated between 359 and 346 Ma by LA-ICP MS and SIMS zircon U-Pb
178 methods (Feng et al. 2014; Zhang et al. 2015; Dong et al. 2018). The Katbasu deposit
179 mainly consists of two types of ores: (1) the vein type Cu-Au ores with pyrite
180 -chalcopyrite veins/veinlets crosscutting or enclosed in the granite (Fig. 3e), and (2)
181 massive Au ores mainly occur as veins that generally have a sharp contact with the
182 host granite or locally replace the granite, and pyrite and quartz as main minerals
183 (Figs. 3g and h). Massive gold ore is the main ore type of the Katbasu deposit,
184 accounting for more than 90% of the total ores. By contrast, the Cu-Au ores are
185 relatively small in scale, and mainly occur in the footwall. The two types of ores are
186 generally spatially separated, though locally small parts of Cu-Au ores are overprinted
187 by massive gold ores. Some Cu-Au mineralization occurred in the contact area where
188 the diorite dikes intruded into the granite pluton (Xing et al. 2016). The massive Au
189 ores mainly occur as tabular or lenses dipping to the south, with the dip angles
190 varying between $\sim 20^\circ$ and 70° . The Cu-Au ores and massive Au ores are nearly
191 parallel. The thickness of the vein type Cu-Au orebody mainly ranges between several
192 centimeters and tens of centimeters, whereas the thickness of the massive Au orebody
193 varies mainly from tens of centimeters to several meters.

194 Pyrite is the predominant ore mineral in the Katbasu Au deposit, and it
195 precipitated in all ore-forming processes (Figs. 4 and 5). Other ore minerals include
196 chalcopyrite, native gold, scheelite, and Te-Bi minerals. The gangue minerals consist

197 of sericite, quartz, rutile, monazite, apatite, and calcite. Gold mainly occurs as native
198 gold in the massive Au and veinlet Cu-Au ores. Minor petzite was found in the veinlet
199 Cu-Au ores. Native gold usually occurs in pyrite and chalcopyrite as inclusions or fills
200 fractures in pyrites, with small amounts of native gold found in the quartz. Native
201 gold grains mainly vary between $\sim 3 \mu\text{m}$ and $40 \mu\text{m}$ in size. There is no obvious
202 difference in the size or fineness of the native gold between the two types of ores. The
203 mineralogy and compositions of the Te-Bi minerals (Fig. 5) have been studied in
204 detail using the scanning electron microscopy (SEM). The Te-Bi minerals, consisting
205 mostly of tetradytmite ($\text{Bi}_2\text{Te}_2\text{S}$), hessite (Ag_2Te), and petzite (Ag_3AuTe_2), are hosted
206 irregularly in pyrite and chalcopyrite fractures and voids.

207 On the basis of the paragenesis, four stages of sulfides are recognized (Fig. 6).
208 Disseminated pyrite (Py1) grains occurring in the granite and are the products of early
209 hydrothermal alterations (Figs. 3d and 4d). Py1 occurs as anhedral crystals with a
210 porous texture filled by quartz and has no genetic associations to gold or copper
211 minerals, which formed prior to mineralization and are attributed to the pre-ore stage
212 (Stage 1). The subsequent Cu-Au mineralization stage (Stage 2) occurred as veins or
213 veinlets that crosscut the granite, and mainly consists of pyrite (Py2), chalcopyrite,
214 native gold, rutile, and monazite (Figs. 3e, 4e, g, and h), as well as some tetradytmite,
215 hessite, and petzite (Figs. 5a-d). Py2 occurs as medium- to coarse-grained, anhedral
216 crystal aggregates that coexists with chalcopyrite and native gold. Monazite is
217 intergrown with the native gold-hosting chalcopyrite crystals. Rutile coexists with
218 chalcopyrite and pyrite grains. Two distinct types of rutile, namely early rutile (Rt1)

219 and late rutile (Rt₂), have been recognized. The main Au ore stage (Stage 3) minerals
220 are dominated by pyrite (Py₃) and quartz, some native gold, as well as minor rutile,
221 scheelite, and apatite (Figs. 4i and 5e). Py₃ occurs as coarse-grained, anhedral crystal
222 aggregates with porous textures filled by quartz and some native gold. The post-ore
223 calcite veins formed away from ores, and are mainly composed of calcite and
224 fine-grained pyrite (Py₄). Py₄ occurs as isolated, and subhedral to euhedral grains
225 with no obvious porous texture (Figs. 3i and 5f).

226

227 **4. Analytical techniques**

228 4.1. Zircon U-Pb dating

229 Zircon grains from the ore-hosting granite (sample KT17-187; Fig. 3a), mafic
230 enclave (sample KT17-197; Fig. 3b), and diorite (sample KT17-9; Fig. 3c) were
231 separated using a conventional magnetic and density technique and hand-picked under
232 a binocular microscope. The selected zircon grains were mounted in epoxy resin.
233 Prior to analyses, all the selected zircon grains were examined with reflected and
234 transmitted light photomicrographs combined with cathodoluminescence (CL) images
235 (Figs. 7 and 8a) to reveal their internal structures. Zircons with a few inclusions or
236 fissures were chosen for U-Pb dating during this study.

237 Zircon U-Pb analyses of ore-hosting granite and mafic enclave were performed
238 using the Cameca IMS 1280 ion microprobe at the Guangzhou Institute of
239 Geochemistry, Chinese Academy of Sciences (GIGCAS). The ellipsoidal spot for
240 zircon U-Pb dating is about 30× 20 μm in size. Detailed operating and data processing

241 procedures are similar to those described by Li et al. (2009). Measured Pb/U ratios
242 were calibrated relative to the zircon standard Plešovice (Sláma et al. 2008).
243 Non-radiogenic Pb was subtracted from the measured Pb isotopic composition using
244 the measured ^{204}Pb and the present-day average terrestrial Pb isotopic composition in
245 the model of Stacey and Kramers (1975). Uncertainties on individual analyses in data
246 tables are reported at a 1σ level. Mean ages for pooled U/Pb (and Pb/Pb) analyses are
247 quoted with 95% confidence interval. Data reduction was carried out using the Isoplot
248 3.00 program (Ludwig 2003).

249 The U-Pb isotopic analyses of the diorite were carried out by a GeolasPro laser
250 ablation system coupled with a multi-collector inductively coupled plasma mass
251 spectrometer (MC-ICP MS) at the Sample Solution Analytical Technology Co., Ltd.
252 (SSATC) in the Hubei province, Wuhan, China. The analytical spot size was about 32
253 μm in diameter. An Agilent 7700e ICP-MS instrument was used to acquire ion-signal
254 intensities, and He was applied as a carrier gas. Zircon sample 91500 was used as the
255 external standard, and zircon standards GJ-1 and Plešovice were used as unknown
256 samples to monitor the stability and accuracy of the acquired U-Pb data. The data
257 selection and calibration were performed by the ICPMSDataCal (Liu et al. 2010).
258 Correction for common Pb was applied using the method described by Andersen
259 (2002). Weighted mean calculations and concordia diagrams were made using the
260 Isoplot 3.00 program (Ludwig 2003).

261

262 4.2 Monazite U-Pb isotopic analyses

263 The monazite-bearing auriferous sample was collected from the veinlet ores
264 (Figs. 3e and 4g). LA-ICP-MS data collection for both ages and trace element
265 abundance was performed simultaneously at the SSATC. Laser sampling was
266 performed using a GeolasPro laser ablation system that consists of a COMPexPro 102
267 ArF excimer laser. An Agilent 7700e ICP-MS instrument was used to acquire
268 ion-signal intensities. Helium was applied as a carrier gas. Argon was used as the
269 make-up gas and mixed with the carrier gas via a T-connector before entering the ICP.
270 The spot size and frequency of the laser were set to 16 μm and 2 Hz, respectively.
271 Monazite standard TRE and 44069 and glass NIST610 were used as external
272 standards for U-Pb dating and trace element calibration, respectively. Each analysis
273 incorporated a background acquisition of approximately 20-30 s followed by 50 s of
274 data acquisition from the sample. An Excel-based software ICPMSDataCal was used
275 to perform off-line selection and integration of background and analyzed signals,
276 time-drift correction, and quantitative calibration for trace element analysis and U-Pb
277 dating (Liu et al. 2010). Concordia diagrams and weighted mean calculations were
278 made using the Isoplot 3.00 program (Ludwig 2003).

279

280 4.3. In situ rutile Raman spectroscopy, Electron microprobe analysis, and SIMS U-Pb
281 dating

282 Although trace elements can be used to discriminate between rutile, anatase, and
283 brookite (Triebold et al. 2011; Plavsa et al. 2018), the most reliable method to
284 distinguish between the three mineral polymorphs is laser Raman spectroscopy

285 (Meinhold 2010). Thus, before U-Pb isotope analysis, Raman spectroscopy was
286 conducted on the rutile sample at 100 - 4000 cm⁻¹ using a LabRam HR800 laser
287 Raman microspectrometer at the IGGCAS. The incident radiation was provided by an
288 argon ion laser with a wavelength of 532 nm and a source power of 44 mW.

289 Major and minor element compositions of the selected rutile grains were
290 determined using a JEOL JXA-8230 electron probe under operating conditions of 15
291 kV, a 2 μm 10 nA beam, a count time of 10 s (peak) and 5 s for the upper and lower
292 background, at the Fuzhou University, Fuzhou, China. Natural and synthetic minerals
293 were used for standard calibration. The ZAF correction method was used to correct
294 the atomic number (Z), absorption (A), and fluorescence (F) effects for all analyzed
295 minerals.

296 Rutile crystals, coexisting with chalcopyrite (Figs. 4b and c), were drilled from
297 the thin section and then mounted in a transparent epoxy together with the DXK rutile
298 standard (²⁰⁶Pb/²³⁸U age = 1782.6 ± 2.8 Ma, Li et al. 2013) and an in-house rutile
299 standard JDX (²⁰⁶Pb/²³⁸U age = 509 ± 8 Ma, Li et al. 2011). The *in-situ* of U - Pb
300 isotope measurements of rutile were performed using a CAMECA IMS-1280 ion
301 microprobe at IGGCAS. The instrumental conditions and measurement procedures
302 were similar to those described by Li et al. (2011). The ellipsoidal spot was about 30
303 × 20 μm in size. Each measurement comprises 10 cycles during a total analytical
304 duration of ~ 15 minutes, including 2 minutes rastering prior to the actual analysis to
305 reduce the contribution of surface Pb contaminants. The DXK rutile was used as the
306 standard to calibrate the Pb/U fractionation, and JDX rutile as an unknown to monitor

307 the whole analytical procedure. The U-Pb isotopic ages were calculated using the
308 decay constants recommended by Sterger and Jäger (1977) and the Isoplot 3.00
309 program (Ludwig 2003).

310

311 **5. Results**

312 5.1 Zircon U-Pb ages

313 Zircon U-Pb dating results of the ore-hosting granite and the mafic enclaves are
314 listed in Table 1. The CL images of representative zircon grains from the ore-hosting
315 granite and mafic enclave are shown in the Figure 7. Based on photomicrographs and
316 CL images, analytical sites with few inclusions or fissures were chosen for U-Pb
317 dating during this study. Most zircon grains from the ore-hosting granite exhibit
318 oscillatory zoning with no obvious rim to core textural differences. They have a
319 prolate axis length of ~80-250 μm , with length/width ratios between 1:1 and 2:1. They
320 yielded high Th/U ratios of 0.57 to 1.10, consistent with a magmatic origin. All ten
321 spot analyses yielded a concordia age of 354.1 ± 1.6 Ma (MSWD=1.8) (Fig. 7a). This
322 age is interpreted as the crystallization age of the ore-hosting granite. Zircon grains
323 from the mafic enclave have darker CL images than those from the granite. They
324 generally show a dark core overgrown by a thin bright rim (Fig. 7b). They have a
325 length of ~60 to 150 μm , with length/width ratios between 1:1 and 1.5:1. Because the
326 rim is too thin to be analyzed, only the cores were analyzed. They have high Th/U
327 ratios of 0.92 to 3.23. Eight spot analyses gave a concordia age of 355.8 ± 1.7

328 Ma (MSWD = 0.68) (Fig. 7b), which is interpreted as the crystallization age of the
329 mafic enclave.

330 Zircon U-Pb dating results of diorite are listed in Table 2. Similar to the mafic
331 enclaves, zircon grains in the diorite generally have a dark core and a thin bright rim.
332 They have a length of ~50-130 μm , with length/width ratios between 1:1 and 2:1.
333 They have Th/U ratios ranging from 0.05 to 1.08. All 18 spot analyses yielded a wide
334 range of $^{206}\text{Pb}/^{238}\text{U}$ ages varying from 349.4 ± 3.2 Ma to 401.2 ± 4.7 Ma. Given the
335 geological fact that the diorite intruded in the granite, the $^{206}\text{Pb}/^{238}\text{U}$ ages older than
336 360 Ma may indicate a mixing in of xenocrystic zircons from the strata during ascent
337 of the magma rather than the crystallization age of the diorite. Fourteen spots with
338 $^{206}\text{Pb}/^{238}\text{U}$ ages older than 360 Ma, varying from 361.9 Ma to 401.2 Ma, define a
339 weighted mean age of 373.7 ± 5.9 Ma (MSWD = 6.3; Fig. 8b). Four spot
340 analyses younger than 360 Ma (Fig. 8c) gave a weighted mean age of 352.0 ± 3.2
341 Ma (MSWD = 0.52; Fig. 8d), which is interpreted as the crystallization age of the
342 diorite.

343

344 5.2 Monazite U-Pb age and trace elements

345 LA-ICP-MS U-Pb dating results are given in Table 3. Monazite is closely
346 associated with gold-hosting chalcopyrite, and the BSE images show that monazite is
347 compositionally homogeneous without observable zoning (Figs. 4g and h). No
348 magmatic monazite was found within the host granite or diorite. Monazite in the ores
349 occurs as elongated or irregular grains from less than 10 to ~100 μm in size. The

350 monazite contains relatively low amounts of Th (494-2790 ppm) and U (308-1494
351 ppm), yielding Th/U ratios of 0.4 to 9.1. These relatively low Th and U content are
352 much lower than the magmatic monazite, but consistent with the compositions of
353 hydrothermal monazite (Fig. 9a; Schandl and Gorton 2004; Taylor et al. 2015).
354 Twenty-seven monazite analyses yielded a concordant $^{206}\text{Pb}/^{238}\text{U}$ age of 348.6 ± 0.9
355 Ma (1σ , MSWD = 3.1; Fig. 9c), with a weighted mean age of 348.7 ± 2.3 Ma (2σ ,
356 MSWD = 1.6; Fig. 9d).

357 The trace element results for monazite are listed in Supplemental Table 1. The
358 monazite samples display relatively coherent LREE enriched and HREE depleted
359 patterns with obvious negative Eu anomalies.

360

361 5.3 In situ rutile Raman analyses, trace elements, and U-Pb age

362 Two types of TiO_2 minerals in the Katbasu ores are characterized by the peaks at
363 wavenumbers 142, 228, 445, and 612 cm^{-1} for Rt1, and 142, 228, 445, and 610 cm^{-1}
364 for Rt2, respectively (Fig. 10c). These spectra are similar with those from rutile, but
365 inconsistent with those from brookite and anatase (Fig. 10d; Meinhold 2010),
366 suggesting the TiO_2 minerals in the Katbasu ores are rutile.

367 The EMPA results for two types of rutile are listed in Supplemental Table 2. The
368 early formed rutile (Rt1) has relatively low TiO_2 content (85.27-90.31 wt.%) but a
369 high WO_3 content varying between 3.57 and 7.09 wt.%. By contrast, the late formed
370 rutile (Rt2) has nearly pure TiO_2 endmember compositions (94.31-99.78 wt.%) with a
371 low WO_3 content ranging from 0.01 to 0.33 wt.%. In addition to TiO_2 and WO_3 , Rt1

372 also contains higher Nb and Fe contents (0.91-5.21 wt.% and 0.36-1.92 wt.%) than
373 those from Rt2 (0.15-1.67 wt.% and 0.04-0.46 wt.%).

374 A total of sixteen measurements were conducted on the selected W-rich Rt1
375 crystals from the Katbasu gold deposit. The U-Pb isotopic data for the analyzed rutile
376 grains are listed in Table 4 and illustrated in Figure 11. The measured U contents vary
377 from 6 to 172 ppm. Regression of the data points on the Tera-Wasserburg plot gives a
378 lower intercept age of 345 ± 27 Ma (MSWD = 3.3). The discordance age of rutile may
379 be caused by mixtures of heterochemical, resolvably diachronous rutile generations in
380 petrologic disequilibrium (Fig. 10; Villa and Hanchar, 2017).

381

382 **6. Discussion**

383 6.1 Age constraints on magmatism and mineralization in the Katbasu Au-Cu deposit

384 Previous zircon U-Pb dating results of magmatic rocks in the Katbasu ore district
385 include ore-hosting granite, granodiorite, and rhyolite, which yielded ages of $359.8 \pm$
386 5.2 Ma to 345.5 ± 2.6 Ma, 355.7 ± 2.7 Ma, and 335.7 ± 1.1 Ma (Feng et al. 2014;
387 Zhang et al. 2015; Dong et al. 2018; Li et al. 2018), respectively. In particular, the
388 zircon U-Pb ages of the ore-hosting granite vary widely from 359.8 ± 5.2 Ma to 345.5
389 ± 2.6 Ma. It is therefore necessary to evaluate the reliability of our age. The
390 geological relations among the granite, mafic enclave, and diorite dike indicates that
391 the mafic enclave and diorite dike were formed before and after the granite,
392 respectively. The zircon U-Pb ages of the mafic enclaves, ore-hosting granite, and
393 diorite obtained in this study are 355.8 ± 1.7 Ma, 354.1 ± 1.6 Ma, and 352.0 ± 3.2 Ma,

394 respectively. This is consistent with the geological facts, indicating that the
395 ore-hosting granite formed at ca. 354 Ma.

396 Gold in Katbasu Au-Cu deposit is mainly hosted in the massive quartz-sulfide
397 ores. Rb-Sr and Re-Os isochron ages of the auriferous pyrite are 322.5 ± 6.8 Ma
398 (Dong et al. 2018) and 310.9 ± 4.2 Ma (Zhang et al. 2015), respectively. These
399 geochronological results show that the formation time of the main gold mineralization
400 is obviously later than that of the ore-hosting granite. However, the formation time of
401 copper mineralization and its possible links to gold mineralization remains poorly
402 understood. The paragenesis of the minerals indicates that chalcopyrite is closely
403 related to native gold, monazite, and rutile in the stockwork ore (Figs. 4e,f,g, and h),
404 indicating a Cu-Au mineralization independent of the main Au mineralization. Thus,
405 if the monazite and rutile were formed by hydrothermal fluids instead of having been
406 inherited from the wall rock granite, the ages of monazite and rutile would represent
407 the timing of Cu-Au mineralization in the Katbasu deposit.

408 Previous studies have shown that magmatic and hydrothermal monazite can be
409 effectively distinguished by their trace elements (Taylor et al. 2015; Zi et al. 2015;
410 Piechocka et al. 2017). The monazite associated with Cu-Au mineralization have
411 relatively low Th and U contents as well as Th/U ratios (Fig. 9a and b), which are
412 consistent with the compositions of hydrothermal monazite but different from those
413 with magmatic origins (Taylor et al. 2015; Piechocka et al. 2017). In addition, no
414 magmatic monazite was found in the Katbasu ore-hosting granite, indicating that the
415 monazite was not inherited from the granite. Thus, we consider that the monazite

416 grains originated from hydrothermal fluids rather than inherited from the ore-hosting
417 granite. To date, there is no effective criteria to distinguish between rutile with a
418 magmatic or hydrothermal origin (Meinhold 2010). The rutile grains associated with
419 the sulfides are W-rich. Tungsten-rich rutile grains have been found in many
420 hydrothermal gold deposits (Dostal et al. 2009; Scott et al. 2011; Agangi et al. 2019).
421 Therefore, we consider that the ages of the monazite and W-rich hydrothermal rutile
422 record the time of Au-Cu mineralization in the Katbasu deposit.

423 The hydrothermal monazite U-Pb age is 348.7 ± 2.3 Ma, which is consistent with
424 the W-rich rutile U-Pb age of 345 ± 27 Ma. These ages are considerably older than
425 the auriferous pyrite Rb-Sr and Re-Os isochron ages of 322.5 ± 6.8 Ma (Dong et al.
426 2018) and 310.9 ± 4.2 Ma (Zhang et al. 2015), indicating an early Cu-Au event before
427 the major Au mineralization event in the Katbasu deposit. In addition, the ages of the
428 hydrothermal monazite and W-rich rutile are also consistent with the zircon U-Pb age
429 of the diorite (352.0 ± 3.2 Ma), suggesting that the early Cu-Au mineralization may
430 be related to diorite. This is further supported by the fact that some Cu-Au
431 mineralization occurred in the contact area where the diorite dikes intruded into
432 granite pluton, and the fact that Cu-Au ores are overprinted by massive Au ores (Xing
433 et al. 2016). Thus, we consider that there was an independent ~ 350 Ma Cu-Au
434 mineralization event before the ~ 315 Ma main mineralization event in the Katbasu
435 deposit.

436 In addition to above mentioned ages, a Sm-Nd isochron age of garnet ($334.3 \pm$
437 6.7 Ma; Liu et al. 2018) in skarn and an $^{40}\text{Ar}/^{39}\text{Ar}$ plateau age for sericite (268.6 ± 1.8

438 Ma; Gao et al. 2015) in the massive Au ore have also been reported in the Katbasu ore
439 district. Geological characteristics show that skarn has no genetic associations with
440 mineralization, and the Sm-Nd isochron age may represent a barren hydrothermal
441 event in the Katbasu deposit. Given the facts that (1) the $^{40}\text{Ar}/^{39}\text{Ar}$ plateau age of
442 sericite is much younger than that of auriferous pyrite (ca. 323-311 Ma; Zhang et al.
443 2015; Dong et al. 2018) in the Katbasu deposit, (2) sericite has low closure
444 temperatures (Chiaradia et al. 2013), and (3) the Katbasu deposit has undergone
445 multi-stage tectonic events (Zhao et al. 2019), we consider that the $^{40}\text{Ar}/^{39}\text{Ar}$ plateau
446 age of sericite may record a post-ore tectonic thermal event in the Katbasu deposit.

447

448 6.2 Genetic type of the Katbasu Au-Cu deposit

449 The Chinese western Tianshan orogenic belt hosts many large epithermal gold
450 deposits (Jinxi-Yelmand, Long et al. 2005; Axi, An and Zhu 2018) as well as
451 orogenic gold deposits (Sawayaerdun, Chen et al. 2012; Wangfeng, Zhang et al. 2012).
452 As a newly discovered large Au-Cu deposit in the western Tianshan, the genetic type
453 of the Katbasu deposit remains controversial, with some researchers relating them to
454 orogenic gold deposits (Zhang et al. 2015; Zhao et al. 2019) and others interpreting
455 them as magmatic-hydrothermal gold deposits (Dong et al. 2018; Liu et al. 2018). The
456 ore genesis of the Katbasu Au-Cu deposit remains debated, partly due to a lack of
457 systematic absolute timing of the complex Au and Cu ore-forming events during the
458 late Paleozoic orogeny in the ore district.

459 As discussed above, an early Cu-Au mineralization (chalcopyrite and minor
460 native gold) and a late Au mineralization (pyrite and native gold) are the two major
461 ore-forming events at the Katbasu deposit. Based on the available rock- and
462 ore-forming ages in the ore district, we consider that there may be two different types
463 of metallogenic events in the Katbasu deposit.

464 The formation time of Cu-Au mineralization (348.7 ± 2.3 Ma) is consistent with
465 the emplacement age of diorite (352.0 ± 3.2 Ma) in the ore district. The Cu-Au
466 mineralization is spatially associated with the diorite, and the diorite in the Katbasu
467 deposit contains some disseminated chalcopyrite and pyrite (Fig. 4a), indicating that it
468 may have provided ore-forming materials. The abundant Cu in the Cu-Au
469 mineralization indicates that it is unlikely to be of orogenic origin because only a
470 small portion of base metals can be released into metamorphic fluids (Zhong et al.
471 2015). Instead, the Cu-Au mineral assemblage is consistent with those in
472 intrusion-related gold deposits (Sillitoe and Thompson 1998). In addition, the age of
473 Cu-Au mineralization is also roughly consistent with the ore formation ages of the
474 Lailisigaoer porphyry Cu-Mo deposit (Molybdenite Re-Os age of 359 ± 8 Ma; Fig. 1b;
475 Li and Chen 2004) and the early stage of Axi epithermal Au deposit (Pyrite Re-Os
476 age of 350 ± 10 Ma; Liu et al. 2020) in the Chinese Western Tianshan. This suggests
477 that the early Cu-Au mineralization could have been of magmatic-hydrothermal origin.
478 The magmatic-hydrothermal Cu-Au ores formed at ~ 350 Ma, corresponding to a
479 subduction environment in the Western Tianshan (Gao et al. 2009; Feng and Zhu
480 2019).

481 By contrast, the major Au mineralization (ca. 323-311 Ma; Zhang et al. 2015;
482 Dong et al. 2018) has no spatial associations with the diorite and it formed much later
483 than any of the magmatic rocks in the ore district (Fig. 12), indicating that the main
484 Au mineralization has no genetic associations with the magmatic rocks in the ore
485 district. In addition, the Au orebodies of the Katbasu deposit is obviously controlled
486 by a fault structure (Fig. 2b), which is consistent with the typical orogenic gold
487 deposits (Goldfarb and Groves 2015; Taylor et al. 2021). Also, the S-Pb isotopes from
488 the main gold ores suggest that the ore-forming metals were derived from crustal
489 materials rather than the granite (Zhang et al. 2015). Moreover, this age is also
490 consistent with the pyrite isochron Re-Os age of the Alastuo granitoid-hosted
491 orogenic deposit (325 ± 3 Ma, Zu et al. 2020) in the Chinese Western Tianshan. This
492 suggests that the main Au mineralization in the Katbasu deposit may belong to the
493 orogenic type. The orogenic Au ores formed during ~323-311 Ma, which corresponds
494 to the tectonic transition period from a subduction to a syn-collision environment in
495 the Western Tianshan (Gao et al. 2009; Zu et al. 2020).

496

497 6.3 A comparison of hydrothermal monazite and rutile geochronology in the gold
498 deposits

499 Monazite and rutile are common accessory minerals in different types of gold
500 deposits, and their U-Pb isotopes are often used to determine the ore formation ages
501 of gold mineralization (Brown et al. 2002; Sarma et al. 2008; Pereira et al. 2019).

502 However, there are few comparative studies on their accuracy and applicability in
503 dating gold deposits.

504 In the granite-hosted Katbasu deposit, monazite and rutile coexist with
505 chalcopyrite and native gold. The BSE images show that the monazite has a
506 homogeneous composition (Figs. 4g and h), whereas the rutile occurs as both an early
507 W-rich rutile and a late rutile (Figs. 10a,b). Monazite trace elements and W-rich rutile
508 replacement textures indicate that they were both formed by hydrothermal fluids
509 (Scott et al. 2011; Taylor et al. 2015). Although they have similar Th/U ratios, the Th
510 and U contents of monazite are much higher than those of rutile (Table 3 and 4). In
511 addition, the U-Pb age of monazite (348.7 ± 2.3 Ma) is consistent with, and more
512 precise than the U-Pb age of rutile (345 ± 27 Ma). Thus, we consider that monazite is
513 more suitable to date the complex mineralization event than rutile in the Katbasu
514 deposit.

515 Other than the Katbasu deposit, the following factors indicate that monazite may
516 be better than rutile in determining the mineralization age of other gold deposits.
517 Rutile is one of three polymorphs, which also include anatase and brookite (Plavsa et
518 al. 2018; Adlakha et al. 2020). In particular, the remobilization of trace elements after
519 the formation of rutile can affect the information on the nature and timing of
520 geological events recorded in rutile (Pe-Piper et al. 2019; Agangi et al. 2020;
521 Verberne et al. 2020). In addition, the TiO₂ mineral polymorphs found in the gold
522 deposits are difficult to distinguish by their geochemical compositions. Laser
523 micro-Raman spectroscopy is a reliable technique to identify rutile (Meinhold 2010),

524 and should be carried out before the U-Pb geochronology. Moreover, the lack of
525 criteria for discriminating hydrothermal rutile makes it difficult to time the formation
526 of gold deposits because rutile is a common accessory mineral in various magmatic,
527 sedimentary, and metamorphic rocks (Zack et al. 2004; Meinhold 2010).

528 By contrast, monazite has no polymorphs. In addition, monazite is chemically
529 and isotopically robust. It can incorporate significant amounts of Th and U as well as
530 exclude common Pb, which makes it a powerful geochronometer (Spear and Pyle
531 2002; Rasmussen et al. 2006). Although monazite can be of magmatic, detrital, and
532 metamorphic origins, hydrothermal monazites can be distinguished by their relatively
533 low Th contents and Th/U ratios as well as their REE patterns (Taylor et al. 2015;
534 Aleinikoff et al. 2016). Therefore, monazite appears to be a better geochronometer
535 than rutile when they both appear in the same gold deposits.

536

537 **7. Implications**

538 Located in the Chinese Western Tianshan, the Katbasu Au-Cu deposit is hosted
539 in a Carboniferous granite intrusion. The main ore types include Cu-Au ores as
540 veinlets crosscutting the granite and Au ores with massive pyrite and quartz as major
541 minerals. Some hydrothermal monazite and rutile grains coexist with chalcopyrite and
542 native gold in the Cu-Au ores. Our new zircon U-Pb results show that the ore-hosting
543 granite formed at ca. 356-354 Ma. The trace element compositions of the monazite
544 suggest it formed from hydrothermal fluids rather than being inherited from the
545 ore-hosting granite. The hydrothermal monazite yielded U-Pb ages of 348.7 ± 2.3 Ma

546 and 345 ± 27 Ma, which are consistent with the zircon U-Pb age of the diorite (352.0
547 ± 3.2 Ma) that intruded the ore-hosting granite. These ages are much older than the
548 auriferous pyrite (ca. 323-311 Ma) in the major Au ores, indicating an early Cu-Au
549 mineralization event prior to the main Au mineralization. The early Cu-Au
550 mineralization could be associated with the diorite and formed by
551 magmatic-hydrothermal fluids. By contrast, the main Au mineralization appear to
552 have formed by metamorphic fluids and could be classified as an orogenic deposit.
553 The results in this study highlight that monazite has the advantages over rutile in
554 dating the complex mineralization ages of hydrothermal gold deposits.

555

556 **Acknowledgments**

557 This research was jointly supported by the National Key Research and
558 Development Program of China (2018YFC0603801 and 2018YFC0604004), National
559 Natural Science Foundation of China (No. 41903042 and No. 42002052), China
560 Postdoctoral Science Foundation (No. 2016LH0003 and No.2017M610984). We
561 thank Ryan Taylor and anonymous reviewer(s) for their thorough and constructive
562 reviews of this paper. Daniel Harlov is thanked for the editorial handling and
563 language polishing.

564

565 **Declaration of interests**

566 The authors declare that they have no known competing financial interests or personal
567 relationships that could have appeared to influence the work reported in this paper.

568

569 **References**

- 570 Adlakha, E. E., Hattori, K., Kerr, M. J., and Boucher B. M., (2020) The origin of
571 Ti-oxide minerals below and within the eastern Athabasca Basin, Canada.
572 American Mineralogist, 105(12), 1875-1888.
- 573 Agangi, A., Reddy, S. M., Plavsa, D., Fougereuse, D., Clark, C., Roberts, M., and
574 Johnson, T. E. (2019) Antimony in rutile as a pathfinder for orogenic gold
575 deposits. Ore Geology Reviews, 106, 1-11.
- 576 Agangi, A., Plavsa, D., Reddy, S. M., Olierook, H., and Kylander-Clark, A. (2020)
577 Compositional modification and trace element decoupling in rutile: Insight from
578 the Capricorn Orogen, Western Australia. Precambrian Research, 345, 105772.
- 579 Aleinikoff, J. N., Selby, D., Slack, J. F., Day, W. C., Pillers, R. M., Cosca, M. A.,
580 Seeger, C. M., Fanning, C. M., and Samson, I. M. (2016) U-Pb, Re-Os, and
581 Ar/Ar Geochronology of Rare Earth Element (REE)-Rich Breccia Pipes and
582 Associated Host Rocks from the Mesoproterozoic Pea Ridge Fe-REE-Au
583 Deposit, St. Francois Mountains, Missouri. Economic Geology, 111(8),
584 1883-1914.
- 585 An, F., and Zhu, Y., (2018) Geology and geochemistry of the Early Permian Axi
586 low-sulfidation epithermal gold deposit in North Tianshan (NW China). Ore
587 Geology Reviews, 100, 12-30.
- 588 Andersen, T. (2002) Correction of common Pb in U-Pb analyses that do not report
589 ²⁰⁴Pb. Chemical Geology, 192, 59-79.

- 590 Bea, F. (1996) Residence of REE, Y, Th and U in granites and crustal protoliths :
591 implications for the chemistry of crustal melts. *Journal of Petrology*, 37(3),
592 521–552.
- 593 Brown, S. M., Fletcher, I. R., Stein, H. J., Snee, L. W., and Groves, D. I. (2002)
594 Geochronological Constraints on Pre-, Syn-, and Postmineralization Events at
595 the World-Class Cleo Gold Deposit, Eastern Goldfields Province, Western
596 Australia. *Economic Geology*, 97(3), 541-559.
- 597 Cabral, A. R., Eugster, O., Brauns, M., Lehmann, B., Rösel, D., Zack, T., de Abreu, F.
598 R., Pernicka, E., and Barth, M. (2013) Direct dating of gold by radiogenic helium:
599 Testing the method on gold from Diamantina, Minas Gerais, Brazil. *Geology*,
600 41(2), 163-166.
- 601 Chen, H. Y., Chen, Y. J., and Baker, M. (2012) Isotopic geochemistry of the
602 Sawayaerdun orogenic-type gold deposit, Tianshan, northwest China:
603 implications for ore genesis and mineral exploration. *Chemical Geology*, 310,
604 1-11.
- 605 Chiaradia, M., Konopelko, D., Seltmann, R., and Cliff, R. A., (2006) Lead isotope
606 variations across terrane boundaries of the Tien Shan and Chinese Altay.
607 *Mineralium Deposita*, 41(5), 411-428.
- 608 Chiaradia, M., Schaltegger, U., Spikings, R., Wotzlaw, J.F., and Ovtcharova, M.
609 (2013) How accurately can we date the duration of magmatic-hydrothermal
610 events in porphyry systems?—an invited paper. *Economic Geology*, 108 (4),
611 565-584.

- 612 Cooke, D. R., Hollings, P., and Walshe, J. L. (2005) Giant porphyry deposits:
613 characteristics, distribution, and tectonic controls. *Economic Geology*, 100(5),
614 801-818.
- 615 Deng, J., Qiu, K.F., Wang, Q.F., Goldfarb, R.J., Yang, L.Q., Zi, J.W., Geng, J.Z., and
616 Ma, Y. (2020) In-situ dating of hydrothermal monazite and implications on the
617 geodynamic controls of ore formation in the Jiaodong gold province, eastern
618 China. *Economic Geology*, 115(3), 671-685.
- 619 Dong, L.L., Wan, B., Yang, W.Z., Deng, C., Chen, Z., Yang, L., Cai, K.D., and Xiao,
620 W.J. (2018) Rb-Sr geochronology of single gold-bearing pyrite grains from the
621 Katbasu gold deposit in the South Tianshan, China and its geological
622 significance. *Ore Geology Reviews*, 100, 99-110.
- 623 Dostal, J., Kontak, D. J., and Chatterjee, A. K., (2009) Trace element geochemistry of
624 scheelite and rutile from metaturbidite-hosted quartz vein gold deposits, Meguma
625 Terrane, Nova Scotia, Canada: genetic implications. *Mineralogy and Petrology*,
626 97(1), 95-109.
- 627 Feng, B., Xue, C., Zhao, X., Ding, Z., Zhang, Q., Zu, B., Yang, W., Lin, Z., and Chen,
628 W. (2014) Petrology, geochemistry and zircon U-Pb isotope chronology of
629 monzogranite of the Katbasu Au-Cu deposit, western Tianshan, Xinjiang
630 Province. *Earth Science Frontiers*, 21, 187-195 (in Chinese with English
631 abstract).

- 632 Feng, W.Y., and Zhu, Y.F. (2018) Petrology and geochemistry of mafic and
633 ultramafic rocks in the north Tianshan ophiolite: Implications for petrogenesis
634 and tectonic setting. *Lithos*, 318, 124-142.
- 635 Feng, W.Y., and Zhu, Y.F. (2019) Petrogenesis and tectonic implications of the late
636 Carboniferous calc-alkaline and shoshonitic magmatic rocks in the Awulale
637 mountain, western Tianshan. *Gondwana Research*, 76, 44-61.
- 638 Fielding, I. O. H., Johnson, S. P., Zi, J. W., Rasmussen, B., Muhling, J. R., Dunkley,
639 D. J., Sheppard, S., Wingate, M. T. D., and Rogers, J. R. (2017) Using in situ
640 SHRIMP U-Pb monazite and xenotime geochronology to determine the age of
641 orogenic gold mineralization: An example from the Paulsens Mine, Southern
642 Pilbara Craton. *Economic Geology*, 112(5), 1205-1230.
- 643 Frimmel, H. E. (2008) Earth's continental crustal gold endowment. *Earth and*
644 *Planetary Science Letters*, 267(1), 45-55.
- 645 Gao, J., Li, M.S., Xiao, X.C., Tang, Y.Q., and He, G.Q. (1998) Paleozoic tectonic
646 evolution of the Tianshan Orogen, northwestern China. *Tectonophysics*, 287
647 (1-4), 213-231.
- 648 Gao, J., Long, L., Klemd, R., Qian, Q., Liu, D., Xiong, X., Su, W., Liu, W., Wang,
649 Y.T., and Yang, F. (2009) Tectonic evolution of the South Tianshan orogen and
650 adjacent regions, NW China: geochemical and age constraints of granitoid rocks.
651 *International Journal of Earth Sciences*, 98(6), 1221-1238.
- 652 Gao, Y.W., Zhang, Z.L., Wang, Z.H., Yang, W.Z., Ban, J.Y., Dong, F.C., and Tan,
653 W.J. (2015) Geochronology of the Katabaasu gold deposit in West Tian Shan and

- 654 its geological significance: evidence from ^{40}Ar - ^{39}Ar isotopic ages of sericite.
655 Geology and Exploration, 5, 805-815 (in Chinese with English abstract).
- 656 Goldfarb, R.J., Snee, L.W., Miller, L.D., and Newberry, R.J. (1991) Rapid dewatering
657 of the crust deduced from ages of mesothermal gold deposits. Nature, 354 (6351),
658 296-298.
- 659 Goldfarb, R. J., and Groves, D. I. (2015) Orogenic gold: Common or evolving fluid
660 and metal sources through time. Lithos, 233, 2-26.
- 661 Grosse, P., Söllner, F., Báez, M. A., Toselli, A. J., Rossi, J. N., and Rosa, J. D. de la.
662 (2009) Lower Carboniferous post-orogenic granites in central-eastern Sierra de
663 Velasco, Sierras Pampeanas, Argentina: U-Pb monazite geochronology,
664 geochemistry and Sr-Nd isotopes. International Journal of Earth Sciences, 98(5),
665 1001-1025.
- 666 Jemielita, R. A., Davis, D. W., and Krogh, T. E. (1990) U-Pb evidence for Abitibi
667 gold mineralization postdating greenstone magmatism and metamorphism.
668 Nature, 346(6287), 831-834.
- 669 Kirk, J., Ruiz, J., Chesley, J., Walshe, J., and England, G. (2002) A Major Archean,
670 Gold- and Crust-Forming Event in the Kaapvaal Craton, South Africa. Science,
671 297(5588), 1856-1858.
- 672 Kusiak, M. A., Williams, I. S., Dunkley, D. J., Konečný, P., Slaby, E., and Martin, H.
673 (2014) Monazite to the rescue: U-Th-Pb dating of the intrusive history of the
674 composite Karkonosze pluton, Bohemian Massif. Chemical Geology, 364,
675 76-92.

- 676 Le Mignot, E., Reisberg, L., André-Mayer, A. S., Bourassa, Y., Fontaine, A., and
677 Miller, J. (2017) Re-Os geochronological evidence for multiple Paleoproterozoic
678 gold events at the scale of the West African craton. *Economic Geology*, 112(1),
679 145-168.
- 680 Li, H.Q., and Chen, F.W. (2004) Isotopic, geochronology of regional mineralization
681 in Xinjiang, China. Geological Publishing House, Beijing, 1-361 (in Chinese
682 with English abstract).
- 683 Li, J. W., Bi, S. J., Selby, D., Chen, L., Vasconcelos, P., Thiede, D., Zhou, M.F., Zhao,
684 X.F., Li, Z.K., and Qiu, H. N. (2012) Giant Mesozoic gold provinces related to
685 the destruction of the North China craton. *Earth and Planetary Science Letters*,
686 349, 26-37.
- 687 Li, Q. L., Lin, W., Su, W., Li, X. H., Shi, Y. H., Liu, Y., and Tang, G. Q. (2011)
688 SIMS U-Pb rutile age of low-temperature eclogites from southwestern Chinese
689 Tianshan, NW China. *Lithos*, 122(1-2), 76-86.
- 690 Li, Q. L., Yang, Y.N., Shi, Y.H., and Lin, W. (2013) Eclogite rutile U-Pb dating:
691 constraint for formation and evolution of continental collisional orogen. *Chinese*
692 *Science Bulletin*, 58, 2279-2284.
- 693 Li, T., Hou, P., and Lin, L., (2018) Geological characteristics and metallogenic
694 environment analysis of the Catabaasu gold copper Deposit: *World Nonferrous*
695 *Metals*, 2018(12), 96-97 (in Chinese with English abstract).
- 696 Li, W., Xie, G., Mao, J., Zhu, Q., and Zheng, J. (2019) Mineralogy, Fluid Inclusion,
697 and Stable Isotope Studies of the Chengchao Deposit, Hubei Province, Eastern

- 698 China: Implications for the Formation of High-Grade Fe Skarn Deposits.
699 Economic Geology, 114(2), 325-352.
- 700 Li, X.H., Liu, Y., Li, Q.L., Guo, C.H., and Chamberlain, K.R. (2009) Precise
701 determination of Phanerozoic zircon Pb/Pb age by multi-collector SIMS without
702 external standardization. *Geochemistry, Geophysics, Geosystems*, 10, Q04010.
- 703 Liu, J.J., Long, X.R., Zheng, M.H., Li, E.D., Wang, J.Z., Sang, H.Q., and Yin, H.X.,
704 (2002) The metallogenic age of Sawaya'erdun gold deposit in southwestern
705 Tianshan mountains, Xinjiang. *Journal of Mineralogy and Petrology*, 22 (3),
706 19-23 (in Chinese with English abstract).
- 707 Liu, Y., Gao, S., Hu, Z., Gao, C., Zong, K., and Wang, D. (2010) Continental and
708 oceanic crust recycling-induced melt-peridotite interactions in the trans-North
709 China Orogen: U–Pb dating, Hf isotopes and trace elements in zircons of mantle
710 xenoliths. *Journal of Petrology*, 51, 537-571.
- 711 Liu, Y., Han, Y., Li, Z., Mo, X., Huang, Y., and Li, Y. (2018) Geological
712 characteristics, deposit type, and metallogenic epoch of the Katebasu
713 gold–copper deposit in western Tianshan. *Geological Journal*, 53, 263-277.
- 714 Liu, Z., Mao, X., Ackerman, L., Li, B., Dick, J. M., Yu, M., Peng, J.T., and Shahzad,
715 S. M., (2020) Two-stage gold mineralization of the Axi epithermal Au deposit,
716 Western Tianshan, NW China: Evidence from Re-Os dating, S isotope, and trace
717 elements of pyrite. *Mineralium Deposita*, 55(5), 863-880.

- 718 Long, X., Hayward, N., Begg, G., Minlu, F., Fangzheng, W., and Pirajno, F. (2005)
719 The Jinxi–Yelmand high-sulfidation epithermal gold deposit, Western Tianshan,
720 Xinjiang Province, P.R. China. *Ore Geology Reviews*, 26(1), 17-37.
- 721 Ludwig, K.R. (2003) User's Manual for Isoplot 3.00 - A Geochronological Toolkit for
722 Microsoft Excel. Berkeley Geochronology Center Special Publication. 4, 1-70.
- 723 Mao, J.W., Konopelko, D., Seltmann, R., Lehmann, B., Chen, W., Wang, Y., Eklund,
724 O., and Usabaliev, T. (2004) Postcollisional age of the Kumtor gold deposit and
725 timing of Hercynian events in the Tien Shan, Kyrgyzstan. *Economic Geology*,
726 99(8), 1771-1780.
- 727 Morelli, R., Creaser, R.A., Seltmann, R., Stuart, F.M., Selby, D., and Graupner, T.
728 (2007) Age and source constraints for the giant Muruntau gold deposit,
729 Uzbekistan, from coupled Re-Os-He isotopes in arsenopyrite: *Geology*, 35 (9),
730 795-798.
- 731 Meinhold, G. (2010) Rutile and its applications in earth sciences. *Earth-Science*
732 *Reviews*, 102(1-2), 1-28.
- 733 Pe-Piper, G., Nagle, J., Piper, D. J. W., and McFarlane, C. R. M. (2019).
734 Geochronology and trace element mobility in rutile from a Carboniferous syenite
735 pegmatite and the role of halogens. *American Mineralogist*, 104(4), 501-513.
- 736 Pereira, I., Storey, C. D., Darling, J., Lana, C. de C., and Alkmim, A. R. (2019) Two
737 billion years of evolution enclosed in hydrothermal rutile: Recycling of the São
738 Francisco Craton Crust and constraints on gold remobilisation processes.
739 *Gondwana Research*, 68, 69-92.

- 740 Piechocka, A. M., Gregory, C. J., Zi, J. W., Sheppard, S., Wingate, M. T. D., and
741 Rasmussen, B. (2017) Monazite trumps zircon: applying SHRIMP U–Pb
742 geochronology to systematically evaluate emplacement ages of leucocratic,
743 low-temperature granites in a complex Precambrian orogeny. Contributions to
744 Mineralogy and Petrology, 172(8), 63.
- 745 Plavsa, D., Reddy, S. M., Agangi, A., Clark, C., Kylander-Clark, A., and Tiddy, C. J.
746 (2018) Microstructural, trace element and geochronological characterization of
747 TiO₂ polymorphs and implications for mineral exploration: Chemical Geology,
748 476, 130-149.
- 749 Rasmussen, B., Fletcher, I. R., Sheppard, S. (2005). Isotopic dating of the migration
750 of a low-grade metamorphic front during orogenesis. Geology, 33(10), 773-776.
- 751 Rasmussen, B., Sheppard, S., and Fletcher, I. R. (2006) Testing ore deposit models
752 using in situ U-Pb geochronology of hydrothermal monazite: Paleoproterozoic
753 gold mineralization in northern Australia. Geology, 34(2), 77-80.
- 754 Sarma, D. S., Mcnaughton, N., Fletcher, I. R., Groves, D., Mohan, M. R., and
755 Balaram, V. (2008) Timing of gold mineralization in the Hutti gold deposit,
756 Dharwar Craton, South India. Economic Geology, 103(8), 1715-1727.
- 757 Schandl E. S., and Gorton M. P. (2004) A textural and geochemical guide to the
758 identification of hydrothermal monazite: criteria for selection of samples for
759 dating epigenetic hydrothermal ore deposits. Economic Geology, 99, 1027-1035.

- 760 Scott, K., Radford, N., Hough, R. M., and Reddy, S. M. (2011) Rutile compositions in
761 the Kalgoorlie Goldfields and their implications for exploration. Australian
762 Journal of Earth Sciences, 58(7), 803-812.
- 763 Selby, D., Creaser, R. A., Hart, C. J. R., Rombach, C. S., Thompson, J. F. H., Smith,
764 M. T., Bakke, A. A., and Goldfarb, R. J. (2002) Absolute timing of sulfide and
765 gold mineralization: A comparison of Re-Os molybdenite and Ar-Ar mica
766 methods from the Tintina Gold Belt, Alaska. *Geology*, 30(9), 791-794.
- 767 Sláma, J., Košler, J., Condon, D.J., Crowley, J.L., Gerdes, A., Hanchar, J.M.,
768 Horstwood, M.S.A., Morrish, G.A., Nasdalai, L., Norbergi, N., and Schaltegger,
769 U. (2008) Plešovice zircon-a new natural reference material for U-Pb and Hf
770 isotopic microanalysis: *Chemical Geology*, 249, 1-35.
- 771 Sillitoe, R. H., and Thompson, J. F. H. (1998) Intrusion-Related Vein Gold Deposits:
772 Types, Tectono - Magmatic Settings and Difficulties of Distinction from
773 Orogenic Gold Deposits. *Resource Geology*, 48(4), 237-250.
- 774 Spear, F.S., and Pyle, J.M. (2002) Apatite, monazite, and xenotime in metamorphic
775 rocks: Geochemical, geobiological, and materials importance. *Reviews in*
776 *Mineralogy and Geochemistry*, 48, 293-335.
- 777 Stacey, J.S., and Kramers, J.D. (1975) Approximation of terrestrial lead isotope
778 evolution by a two-stage model. *Earth and Planetary Science Letters*, 26,
779 207-221.

- 780 Steiger, R. H., and Jäger, E. (1977) Subcommission on geochronology: Convention
781 on the use of decay constants in geo- and cosmochronology. *Earth and Planetary*
782 *Science Letters*, 36(3), 359-362.
- 783 Stein, H. J., Morgan, J. W., and Scherstén, A. (2000) Re-Os Dating of Low-Level
784 Highly Radiogenic (LLHR) Sulfides: The Harnäs Gold Deposit, Southwest
785 Sweden, Records Continental-Scale Tectonic Events. *Economic Geology*, 95(8),
786 1657-1671.
- 787 Stein, H. J. (2014) Dating and Tracing the History of Ore Formation. *Treatise on*
788 *Geochemistry*, 13, 87-118.
- 789 Taylor, R. D., Goldfarb, R. J., Monecke, T., Fletcher, I. R., Cosca, M. A., and Kelly,
790 N. M. (2015) Application of U-Th-Pb Phosphate Geochronology to Young
791 Orogenic Gold Deposits: New Age Constraints on the Formation of the Grass
792 Valley Gold District, Sierra Nevada Foothills Province, California. *Economic*
793 *Geology*, 110(5), 1313-1337.
- 794 Taylor, R. D., Monecke, T., Reynolds, T. J., and Monecke, J. (2021) Paragenesis of
795 an Orogenic Gold Deposit: New Insights on Mineralizing Processes at the Grass
796 Valley District, California. *Economic Geology*, 116(2), 323-356.
- 797 Triebold, S., Luvizotto, G. L., Tolosana-Delgado, R., Zack, T., and Eynatten, H. von.
798 (2011) Discrimination of TiO₂ polymorphs in sedimentary and metamorphic
799 rocks. *Contributions to Mineralogy and Petrology*, 161(4), 581–596.
- 800 Verberne, R., Reddy, S. M., Saxey, D. W., Fougereuse, D., Rickard, W. D. A., Plavska,
801 D., Agangi, A., and Kylander-Clark, A. R. C. (2020) The geochemical and

- 802 geochronological implications of nanoscale trace-element clusters in rutile.
803 *Geology*, 48(11), 1126-1130.
- 804 Villa, I. M., and Hanchar, J. M. (2017). Age discordance and mineralogy. *American*
805 *Mineralogist*, 102(12), 2422-2439.
- 806 White, N. C. (2007) Exploring in China: the challenges and rewards. *SEG Newsletter*,
807 70(1), 8-15.
- 808 Xing, L., Zang, M., Yang, W.Z., Song, A., Lin, Z.H., Chen, W., and Ma, Y. (2016).
809 Discovery of the mineralization diorite in Katebaasu gold-copper deposit,
810 Xinjiang and its geological significance. *Xinjiang Geology*, 34(2), 211-217 (in
811 Chinese with English abstract).
- 812 Xing, L., Xue, C., Zang, M., Yang, W.Z., Zhao, X., Song, A., Lin, Z.H., Zhang, Q.,
813 and Feng, B. (2018) Element distribution of Katebasu gold-copper deposit in
814 West Tianshan Mountains and its exploration significance. *Mineral Deposits*,
815 37(1), 105-115 (in Chinese with English abstract).
- 816 Xue, C.J., Zhao, X.B., Mo, X.X., Dong, L.H., Gu, X.X., Nurtaev, B., Pak, N., Zhang,
817 Z.C., and Wang, X. (2014) Asian Gold Belt in western Tianshan and its dynamic
818 settings, metallogenic control and exploration: *Earth Science Frontiers*, 21,
819 128-155 (in Chinese with English abstract).
- 820 Yang, W., Xue, C., Zhao, X., Zhao, S., Wei, J., Feng, B., Zhou, H., Lin, Z., Zheng, H.,
821 Liu, J., Zhang, Q., and Zu, B. (2013) The discovery of the Kateba'asu large
822 Au-Cu deposit in Xinyuan County, western Tianshan, Xinjiang: *Geological*
823 *Bulletin of China*, 32, 1613-1620 (in Chinese with English abstract).

- 824 Yakubchuk, A.S., Shatov, V.V., Kirwin, D., Tomurtogoo, O., Badarch, G., and
825 Buryak, A.A., (2005) Gold and base metal metallogeny of the central Asian
826 orogenic supercollage. *Economic Geology* 100th Anniversary Volume.
827 1035-1068.
- 828 Zack, T., Eynatten, H. von, and Kronz, A. (2004) Rutile geochemistry and its
829 potential use in quantitative provenance studies. *Sedimentary Geology*, 171(1),
830 37-58.
- 831 Zhai, D., Williams-Jones, A. E., Liu, J., Selby, D., Li, C., Huang, X.-W., Qi, L., and
832 Guo, D. (2019) Evaluating the Use of the Molybdenite Re-Os Chronometer in
833 Dating Gold Mineralization: Evidence from the Haigou Deposit, Northeastern
834 China. *Economic Geology*, 114(5), 897-915.
- 835 Zhai, W., Sun, X., Sun, W., Su, L., He, X., and Wu, Y. (2009) *Geology, geochemistry,*
836 *and genesis of Axi: A Paleozoic low-sulfidation type epithermal gold deposit in*
837 *Xinjiang, China. Ore Geology Reviews*, 36(4), 265-281.
- 838 Zhang, L., Chen, H., Chen, Y., Qin, Y., Liu, C., Zheng, Y., and Jansen, N. H. (2012)
839 *Geology and fluid evolution of the Wangfeng orogenic-type gold deposit,*
840 *Western Tian Shan, China. Ore Geology Reviews*, 49, 85-95.
- 841 Zhang, Q., Xue, C., Zhao, X., Feng, B., Xing, H., Mo, X., Zhao, S., Yang, W., and
842 Xing, L. (2015) *Geology, geochemistry, and metallogenic epoch of the Katebasu*
843 *large-sized gold deposit, Western Tianshan Mountains, Xinjiang. Geology in*
844 *China*, 42, 411-438 (in Chinese with English abstract).

- 845 Zhao, W., Zhao, X., Xue, C., Symons, D. T. A., Cui, X., and Xing, L. (2019)
846 Structural characterization of the Katebasu gold deposit, Xinjiang, China:
847 Tectonic correlation with the amalgamation of the western Tianshan. Ore
848 Geology Reviews, 107, 888-902.
- 849 Zheng, J.H., Mao, J.W., Yang, F.Q., Chai, F.M., and Liu, F. (2016) Newly discovered
850 native gold and bismuth in the Cihai iron-cobalt deposit, eastern Tianshan,
851 Northwest China: Acta Geological Sinica-English Edition, 90(3), 928-938.
- 852 Zheng, J.H., Shen, P., and Li, C.H. (2020) Ore genesis of Axi post-collisional
853 epithermal gold deposit, western Tianshan, NW China: Constraints from U–Pb
854 dating, Hf isotopes, and pyrite in situ sulfur isotopes. Ore Geology Reviews, 117,
855 103290.
- 856 Zhong, R., Brugger, J., Tomkins, A. G., Chen, Y., and Li, W. (2015) Fate of gold and
857 base metals during metamorphic devolatilization of a pelite. Geochimica et
858 Cosmochimica Acta, 171, 338-352.
- 859 Zhu, Y.F., Guo, X., Song, B., Zhang, L.F., and Gu, L.B. (2009) Petrology, Sr–Nd–Hf
860 isotopic geochemistry and zircon chronology of the Late Palaeozoic volcanic
861 rocks in the southwestern Tianshan Mountains, Xinjiang, NW China. Journal of
862 the Geological Society, 166(6), 1085-1099.
- 863 Zhu, Y.F. (2011) Zircon U-Pb and muscovite $^{40}\text{Ar}/^{39}\text{Ar}$ geochronology of the
864 gold-bearing Tianger mylonitized granite, Xinjiang, northwest China:
865 Implications for radiometric dating of mylonitized magmatic rocks. Ore Geology
866 Reviews, 40(1), 108-121.

867 Zhu, Y.F., An, F., Feng, W.Y., and Zhang, H.C. (2016) Geological evolution and
868 huge ore-forming belts in the core part of the Central Asian Metallogenic region.
869 Journal of Earth Science, 27, 491-506.

870 Zi, J.W., Rasmussen, B., Muhling, J. R., Fletcher, I. R., Thorne, A. M., Johnson, S. P.,
871 Cutten, H. N., Dunkley, D. J., and Korhonen, F. J. (2015) In situ U-Pb
872 geochronology of xenotime and monazite from the Abra polymetallic deposit in
873 the Capricorn Orogen, Australia. Dating hydrothermal mineralization and fluid
874 flow in a long-lived crustal structure: Precambrian Research, 260, 91-112.

875 Zu, B., Xue, C., Seltmann, R., Dolgoplova, A., Chi, G., and Li, C. (2020) Geology,
876 geochronology, and S-Pb-Os geochemistry of the Alastuo gold deposit, West
877 Tianshan, NW China. Mineralium Deposita, 55(7), 1-18.

878

879

880 **Figure Captions**

881 Figure 1. (a) Simplified geological map of the Tianshan orogenic belt showing the
882 main tectonic units and gold deposits (modified from Mao et al. 2004; Yakubchuk et
883 al. 2005; Xue et al. 2014). (b) Simplified geological map of the Chinese Western
884 Tianshan showing the main tectonic units as well as iron, copper, and gold deposits
885 (modified from Zheng et al. 2020).

886

887 Figure 2. Geological characteristics of the Katbasu Au-Cu deposit in the Western
888 Tianshan (modified from Yang et al. 2013). (a) Regional geological map of the

889 Katbasu Au-Cu deposit. (b) Geological map showing the distributions of orebodies,
890 magmatic rocks and strata in the Katbasu Au-Cu deposit. (c) Cross-section diagram of
891 the representative exploration line of the Katbasu gold deposit.

892

893 Figure 3. Representative photos showing major types of rocks and ores in the Katbasu
894 Au-Cu deposit. (a) Hand specimen of granite, which consists of potassium feldspar,
895 quartz, plagioclase, and biotite. (b) Hand specimen of mafic enclave in the granite.
896 The mafic enclaves have relatively homogenous mineral sizes and textures from their
897 rims to cores. (c) Hand specimen of diorite, which consists mainly of plagioclase and
898 amphibole. (d) Disseminated pyrite in the hydrothermally altered granite. (e)
899 Pyrite-chalcopyrite veins, associated with chlorite and sericite alterations, crosscut the
900 granite. (f) The granite was replaced by pyrite-quartz veins. (g) Pyrite-quartz vein in
901 the massive sulfide ore. (h) Massive sulfide ore consisting mainly of pyrite and minor
902 quartz. (i) Post-ore calcite veins that crosscut the Au mineralization with a small
903 amount of disseminated pyrites.

904 Mineral abbreviations: Py = pyrite, Cpy = chalcopyrite, Qtz = quartz, Cc = calcite.

905

906 Figure 4. Representative photomicrographs and BSE images of rutile, monazite, and
907 ore minerals in the Katbasu Au-Cu deposit. (a) Amphibole, plagioclase, magnetite,
908 and disseminated pyrite and chalcopyrite in the diorite, reflected light. (b) and (c)
909 Rutile coexists with chalcopyrite in the Cu-Au ores, reflected light. (d) Disseminated
910 pyrite (Py1) in the granite. The pyrite shows a homogeneous texture without zoning,

911 and it has no genetic associations to the gold or copper minerals. (e) Pyrite (Py2),
912 chalcopyrite, and native gold in the sulfide veins that crosscut the granite. (f)
913 Chalcopyrite grains coexist with native gold grains. (g) and (h) Intergrowth of
914 chalcopyrite and monazite in sulfide veins. (i) Pyrite (Py3), scheelite, apatite, and
915 quartz in massive ores. Apatite crystals are not visible because of the brightness and
916 contrast settings.

917 Mineral abbreviations: Py = pyrite, Cpy = chalcopyrite, Pl = plagioclase, Amp =
918 amphibole, Mt = magnetite, Rt = rutile, Au = native gold, Mnz = monazite, Sch =
919 scheelite, Ap = apatite, Qtz = quartz.

920

921 Figure 5. Representative BSE images of ore minerals in the Katbasu Au-Cu deposit.

922 (a) Pyrite, chalcopyrite, native gold, and Te-Bi minerals in the Au-Cu ores. Native
923 gold and Te-Bi minerals occur in the chalcopyrite veins. (b) A close-up view of
924 tetradymite in the chalcopyrite vein in the Fig.a. (c) A close-up view of native gold in
925 the chalcopyrite vein in Fig. 5a. (d) A close-up view of hessite and petzite in the
926 chalcopyrite vein in Fig. 5a. (e) Pyrite (Py3), scheelite, and quartz in massive Au ores.
927 The composition of the pyrite is homogeneous without obvious zoning. (f)
928 Disseminated pyrite (Py4) in post-ore calcite veins.

929 Mineral abbreviations: Py = pyrite, Cpy = chalcopyrite, Au = native gold, Sch =
930 scheelite, Qtz = quartz.

931

932 Figure 6. A mineral association diagram of the Katbasu Au-Cu mineralization. The

933 line thickness represents the relative abundance of minerals.

934

935 Figure 7. SIMS zircon U-Pb concordia diagrams for granite (a) and mafic enclave (b)
936 from the Katbasu Au-Cu deposit.

937

938 Figure 8. (a) LA-ICP-MS U-Pb age of diorite in the Katbasu Au-Cu deposit.
939 Combined with the geological fact that diorite intruded into granite and the
940 crystallization age of the granite is ~ 356 Ma, the zircon older than 356 Ma in the
941 diorite is considered to be xenocrystic zircon captured from the strata during its
942 ascending process. Therefore, only zircons with ages of less than 356 Ma in figure 8c
943 and 8d represent the crystallization age of diorite. Because the rim is too thin to be
944 analyzed, we only analyzed the cores. (b) The weighted mean $^{206}\text{Pb}/^{238}\text{U}$ age of
945 inherited zircon grains in the diorite. (c) The concordia diagram for magmatic zircon
946 grains from the diorite. (d) The weighted mean $^{206}\text{Pb}/^{238}\text{U}$ age of the magmatic zircon
947 grains from the diorite.

948

949 Figure 9. (a) Concentrations of Th versus Th/U ratios for monazite grains that coexist
950 with chalcopyrite from the Katbasu Au-Cu deposit. No magmatic monazite was found
951 in the granite. The hydrothermal and igneous monazite data are from Taylor et al.
952 (2015). (b) The contents of Th versus U for monazite from the Katbasu Au-Cu deposit.
953 The hydrothermal monazite data are from Rasmussen et al. (2005) and Zi et al. (2015),
954 and the magmatic monazite data are from Bea (1996), Grosse et al. (2009), Kusiak et

955 al. (2014), and Piechocka et al. (2017). (c) The concordia diagram for hydrothermal
956 monazite from the Katbasu deposit. (d) The weighted mean $^{206}\text{Pb}/^{238}\text{U}$ age of
957 hydrothermal monazite from the Katbasu deposit.

958

959 Figure 10. (a) and (b) Representative BSE images of early formed W-rich rutile grains
960 (Rt1) and later formed rutile grains (Rt2) that coexist with chalcopyrite in the Katbasu
961 Au-Cu deposit. (c) Raman spectra of Rt1 and Rt2 from the Katbasu Au-Cu deposit. (d)
962 Comparison of Raman spectra among the brookite, anatase, and rutile (Meinhold,
963 2010).

964

965 Figure 11. A Tera-Wasserburg plot for U-Pb data from W-rich rutile grains from the
966 Katbasu Au-Cu deposit.

967

968 Figure 12. A summary of the timing of mineralization, hydrothermal alteration, and
969 magmatism in the Katbasu ore field. In addition to the age data from this study, other
970 age data are from Zhang et al. (2014), Gao et al. (2015), Zhang et al. (2015), Dong et
971 al. (2018), Li et al., (2018), and Liu et al. (2018).

972

973 **Table Captions**

974 Table 1. Zircon SIMS U-Pb isotopic results for the Katbasu granite and mafic
975 enclave.

976

977 Table 2. Results from LA-MC-ICP MS zircon U-Pb dating of diorite in the Katbasu

978 Au-Cu deposit.

979

980 Table 3. Results from LA-MC-ICP MS U-Pb dating of hydrothermal monazites in the

981 Katbasu Au-Cu deposit.

982

983 Table 4. Results from SIMS U-Pb dating of W-rich rutile in the Katbasu Au-Cu

984 deposit.

Figure 1

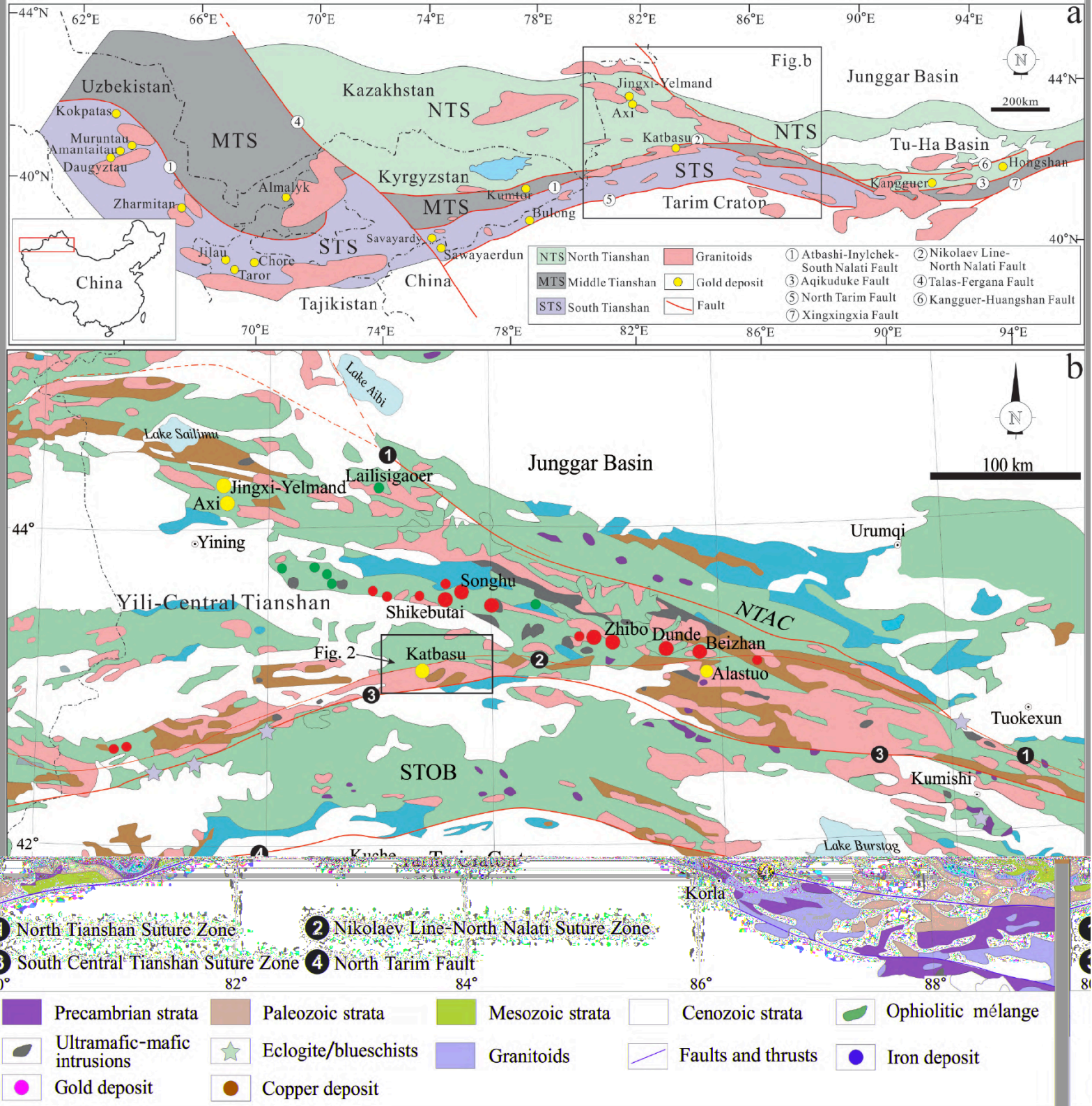


Figure 2

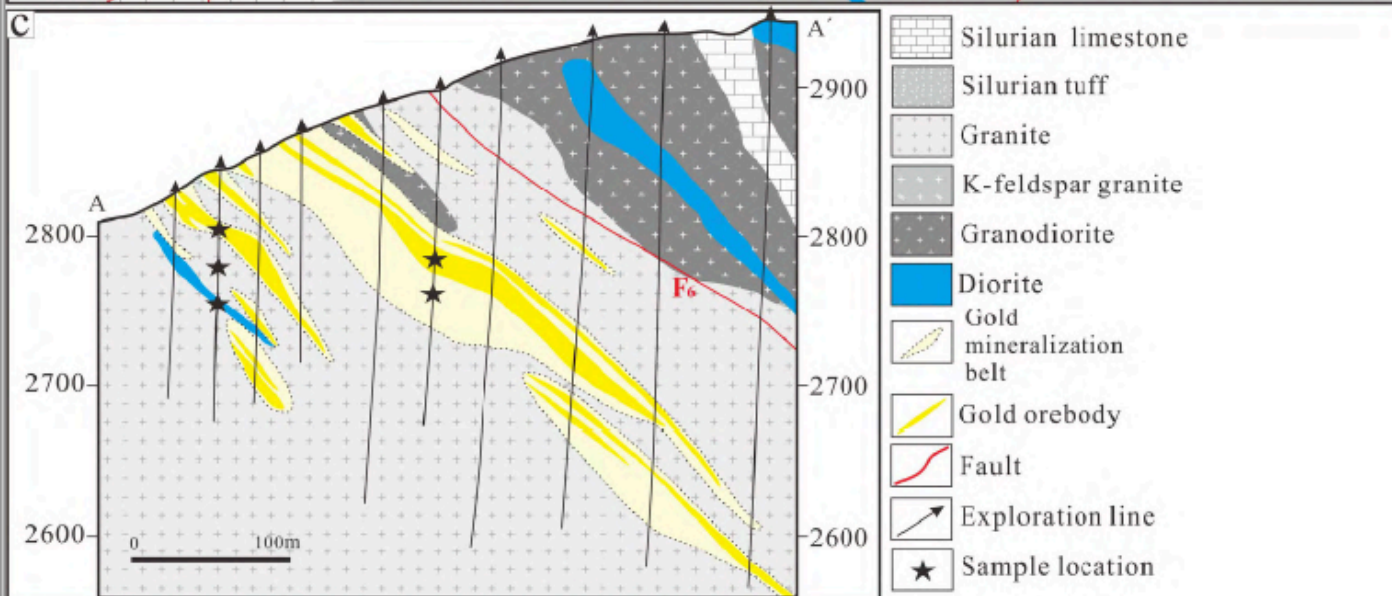
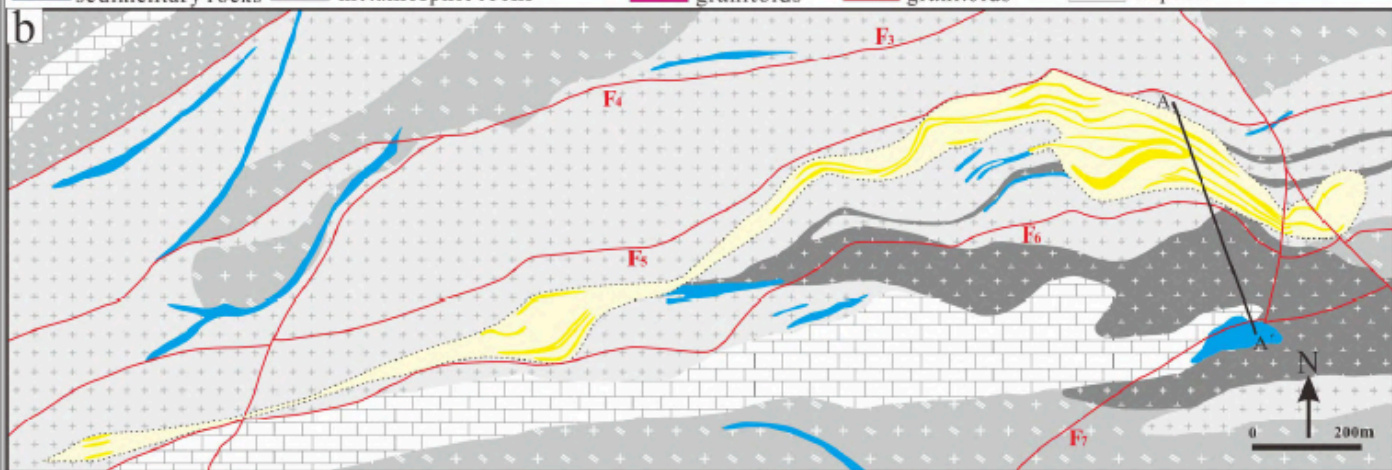
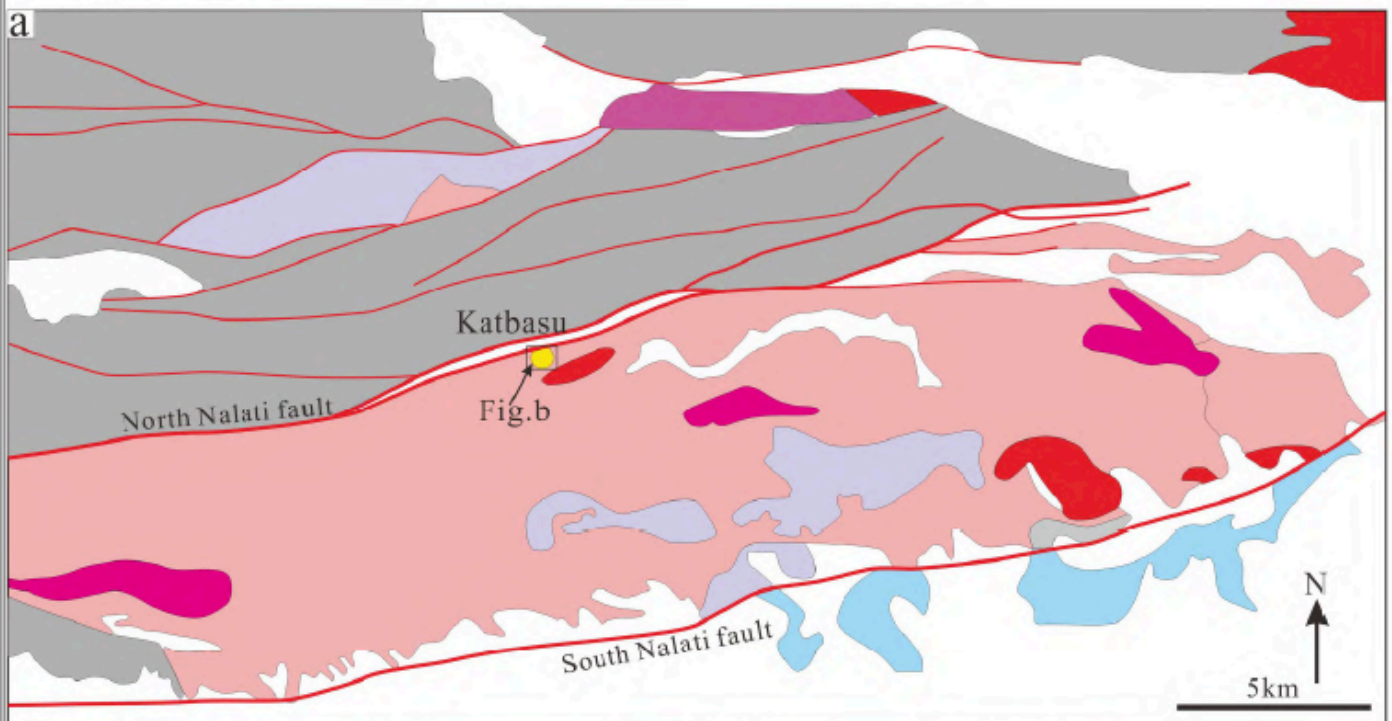


Figure 3

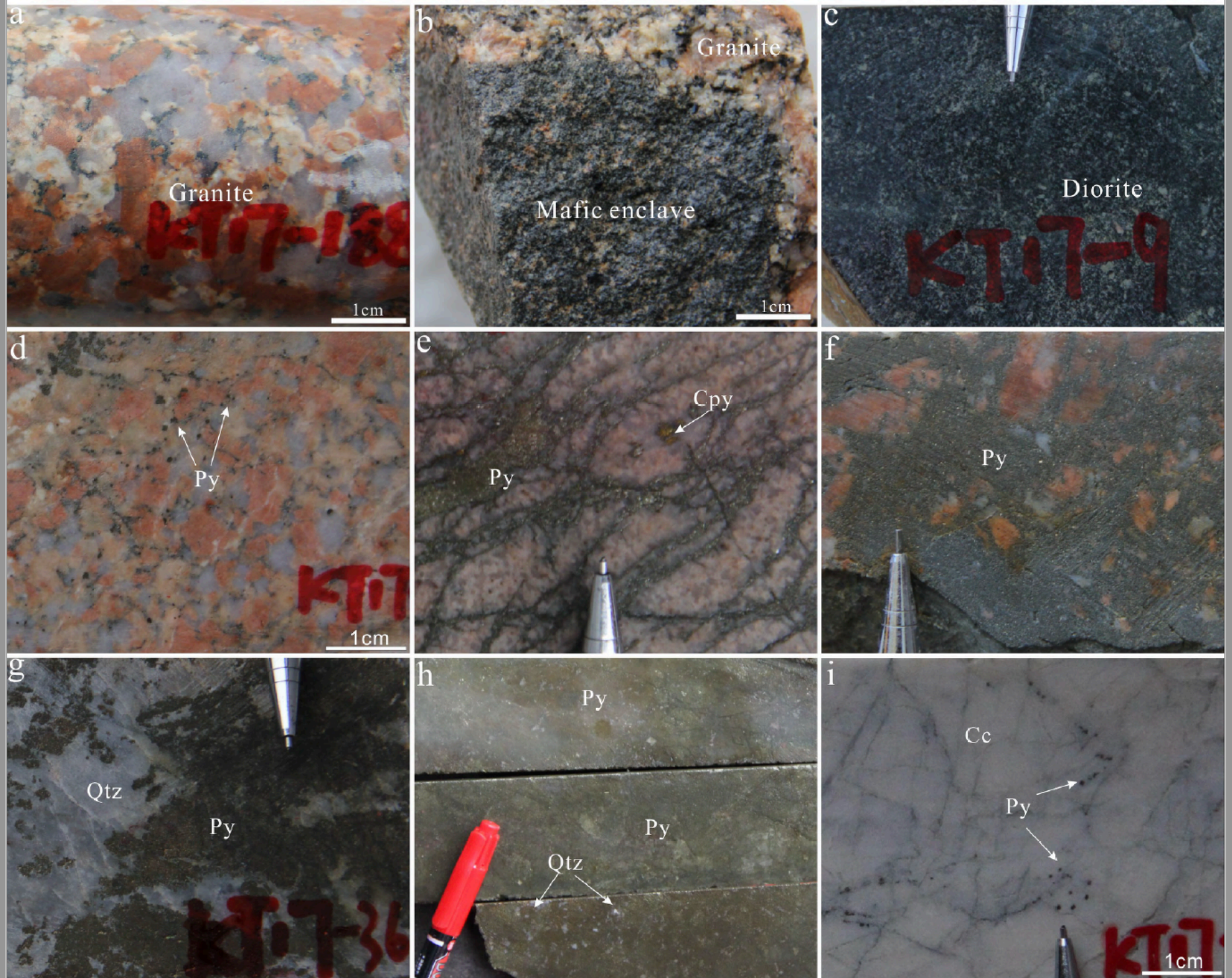


Figure 4

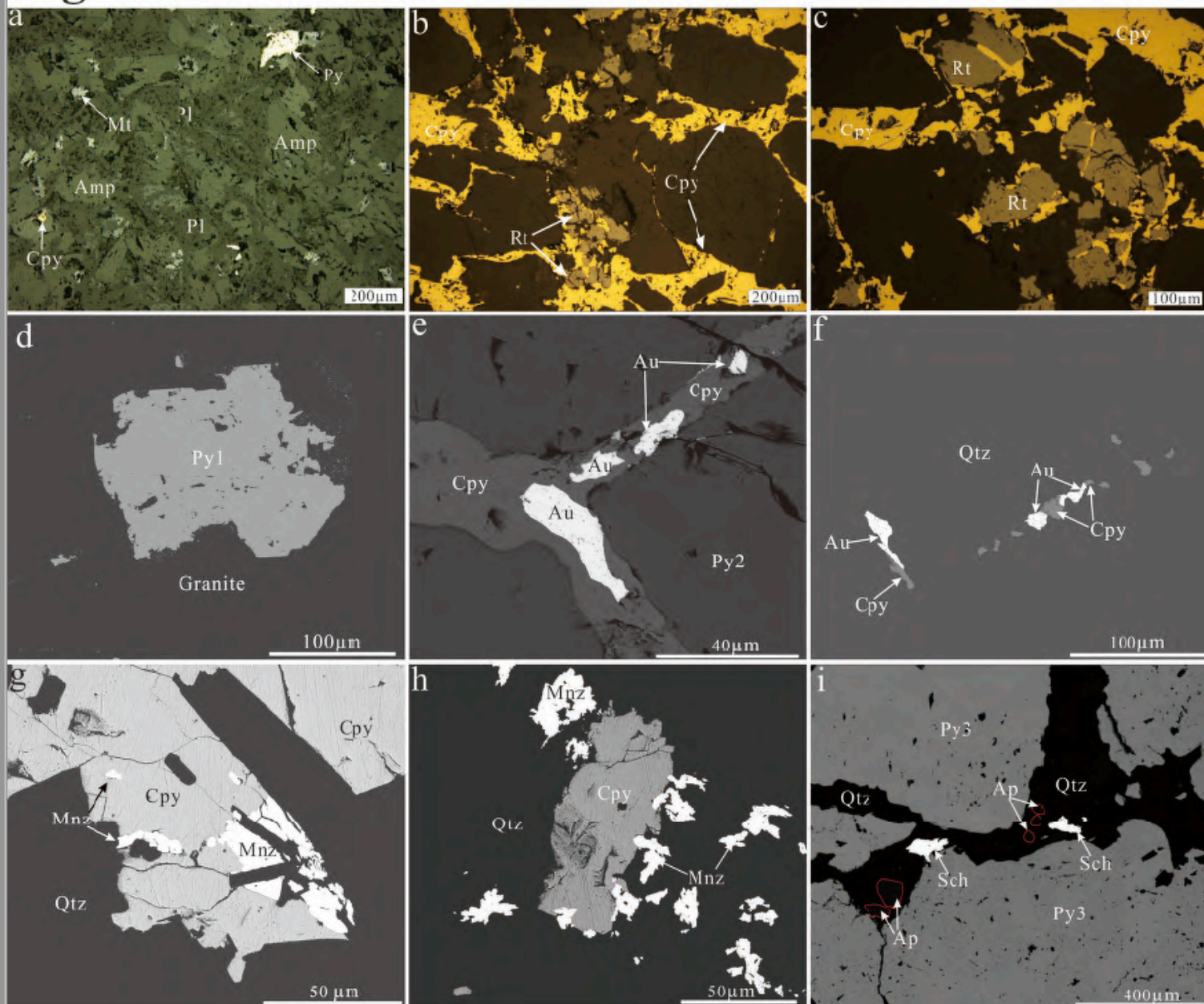


Figure 5

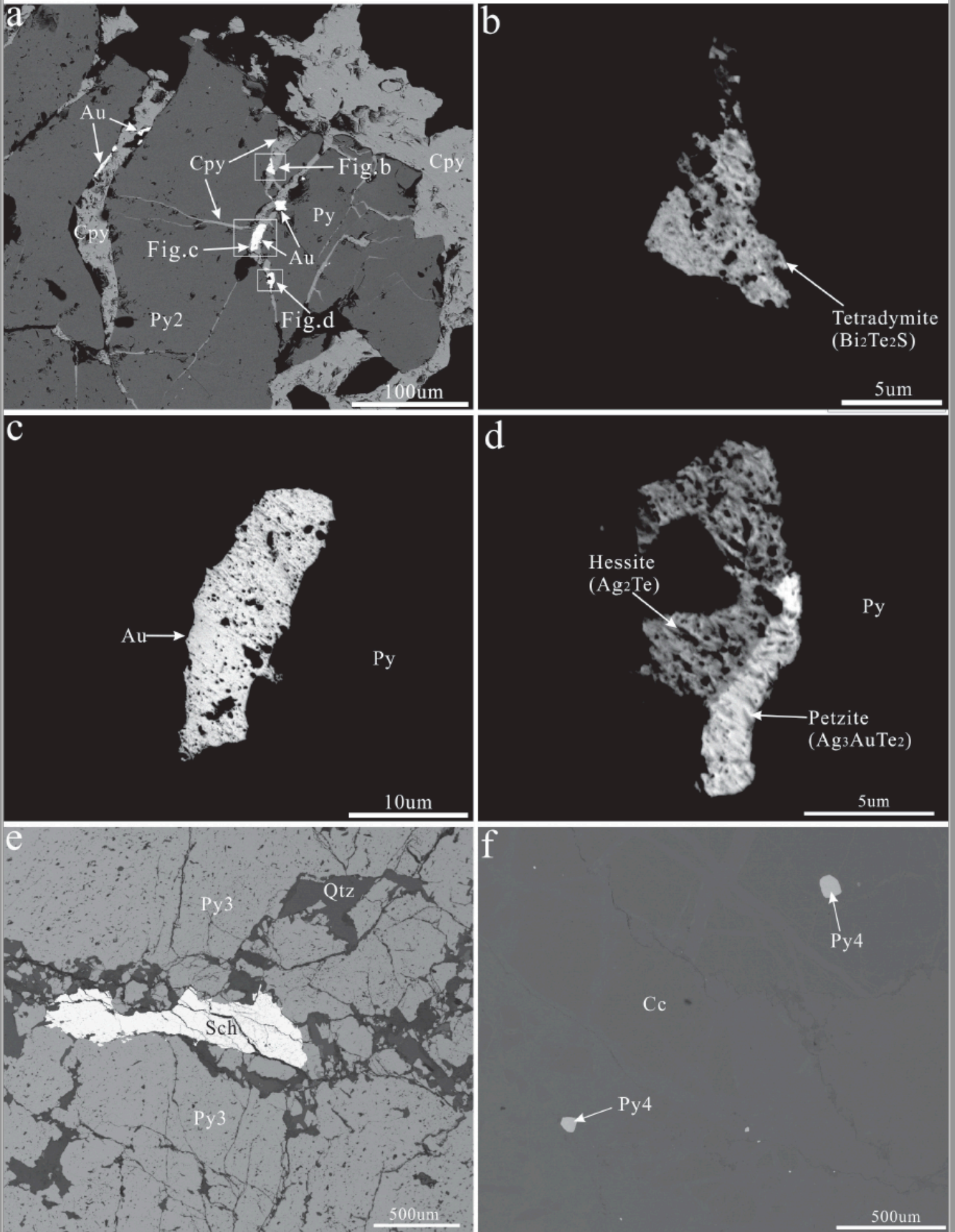


Figure 6

Stage Mineral	(1) Pre-ore stage	(2) Cu-Au mineralization stage	(3) Au mineralization stage	(4) Post-ore stage
Sericite	Py1	Py2	Py3	Py4
Pyrite				
Quartz				
Chalcopyrite				
Rutile				
Native gold				
Apatite				
Monazite				
Tetradymite				
Hessite				
Petzite				
Scheelite				
Calcite				

Figure 7

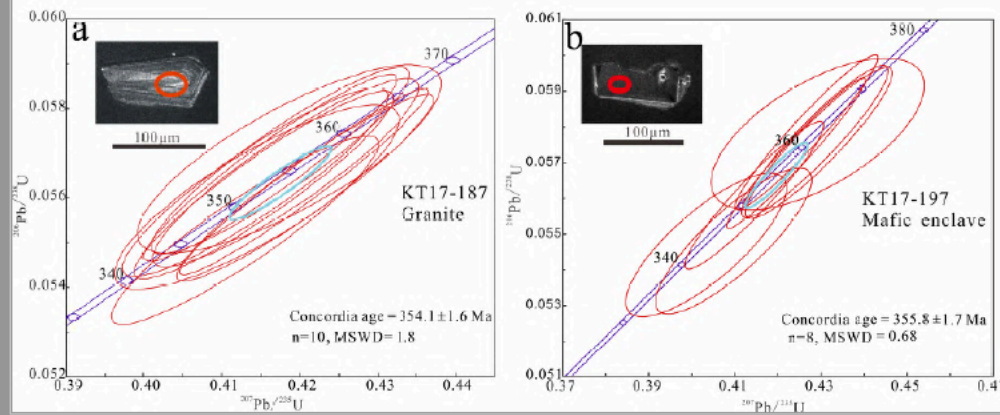


Figure 8

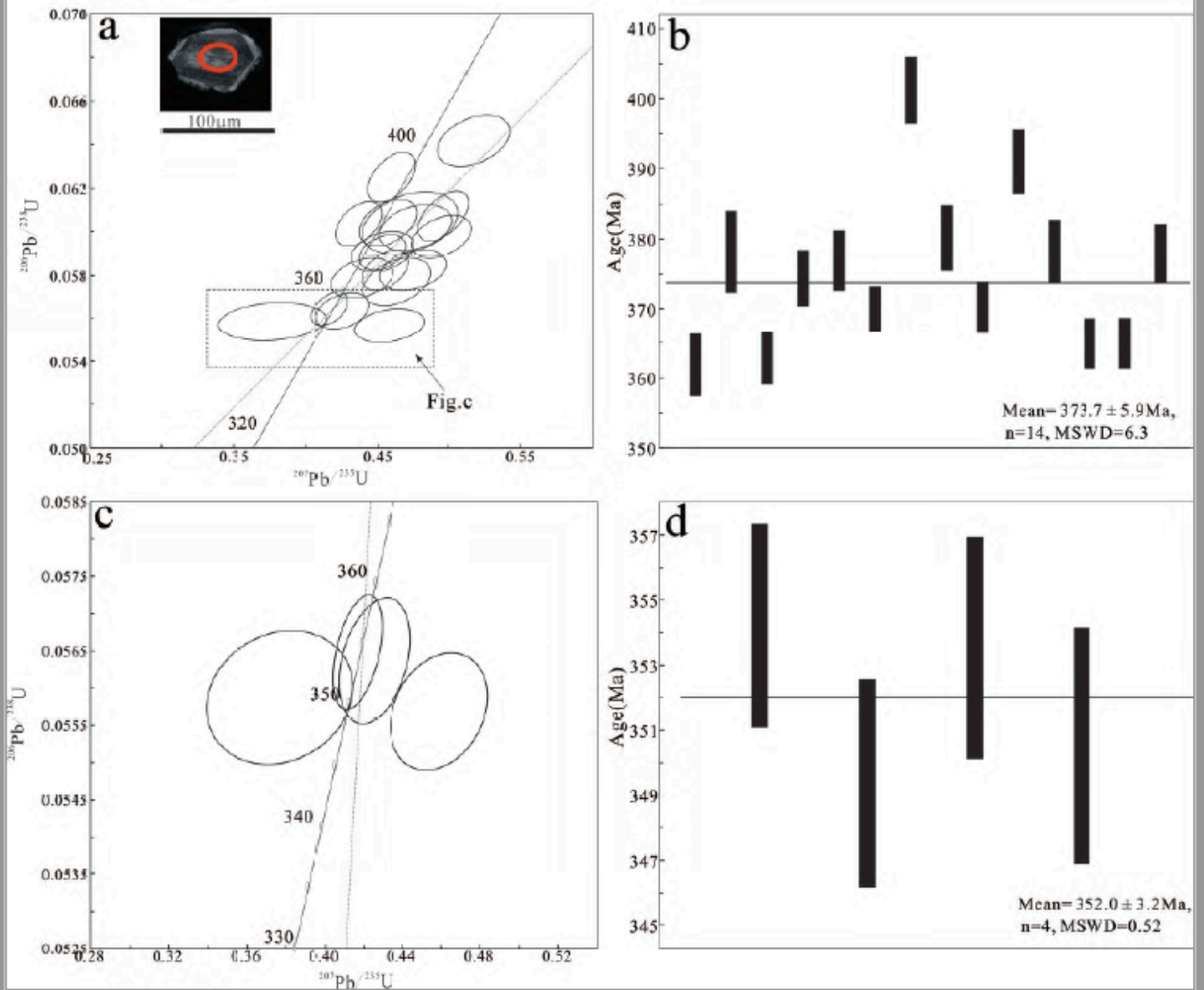


Figure 9

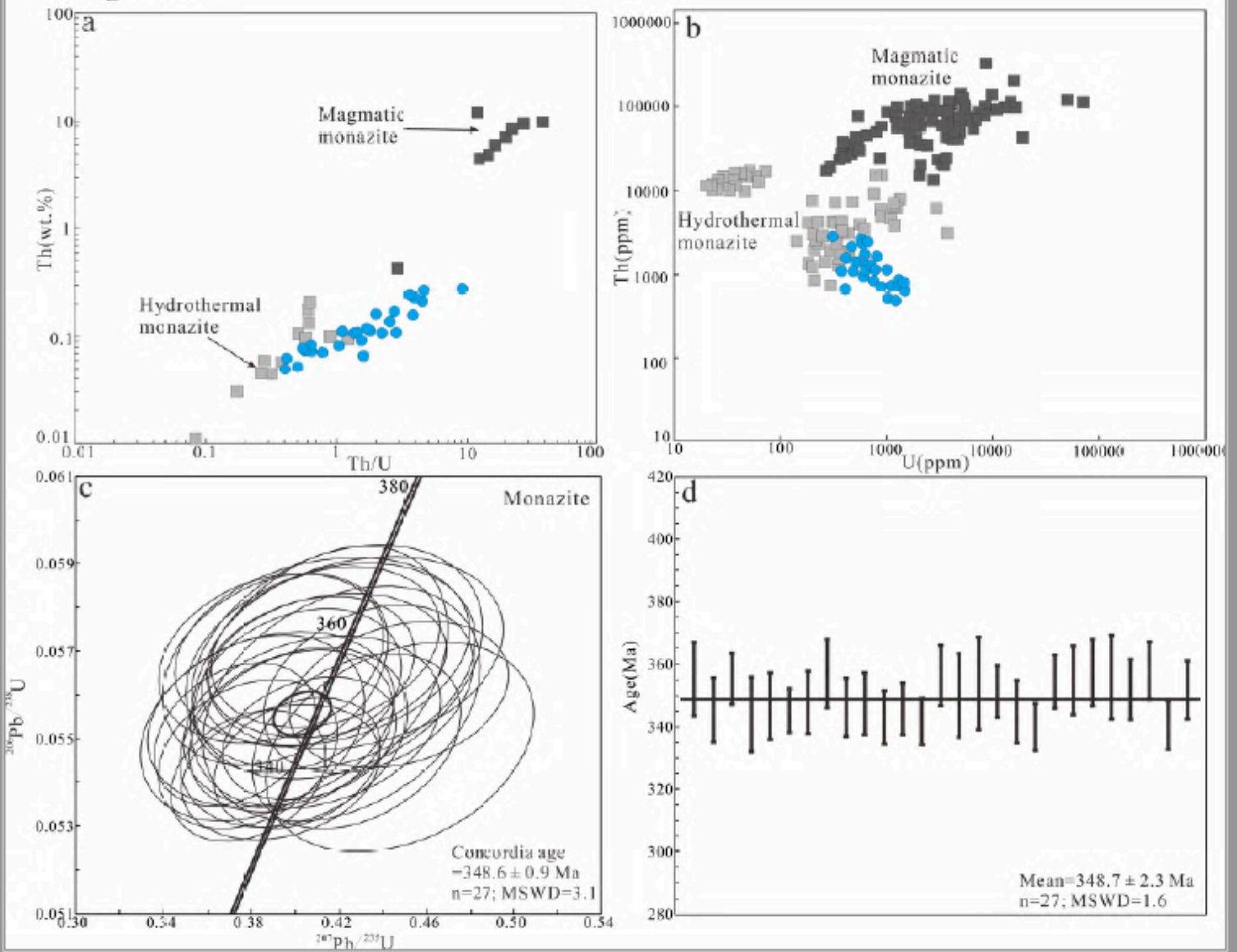


Figure 10

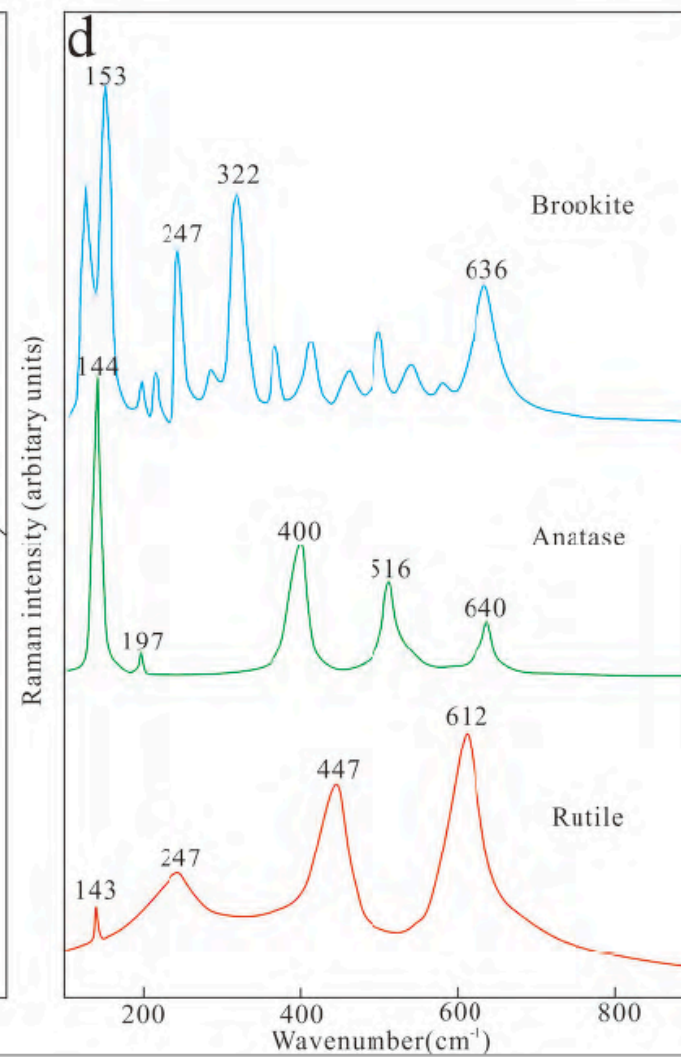
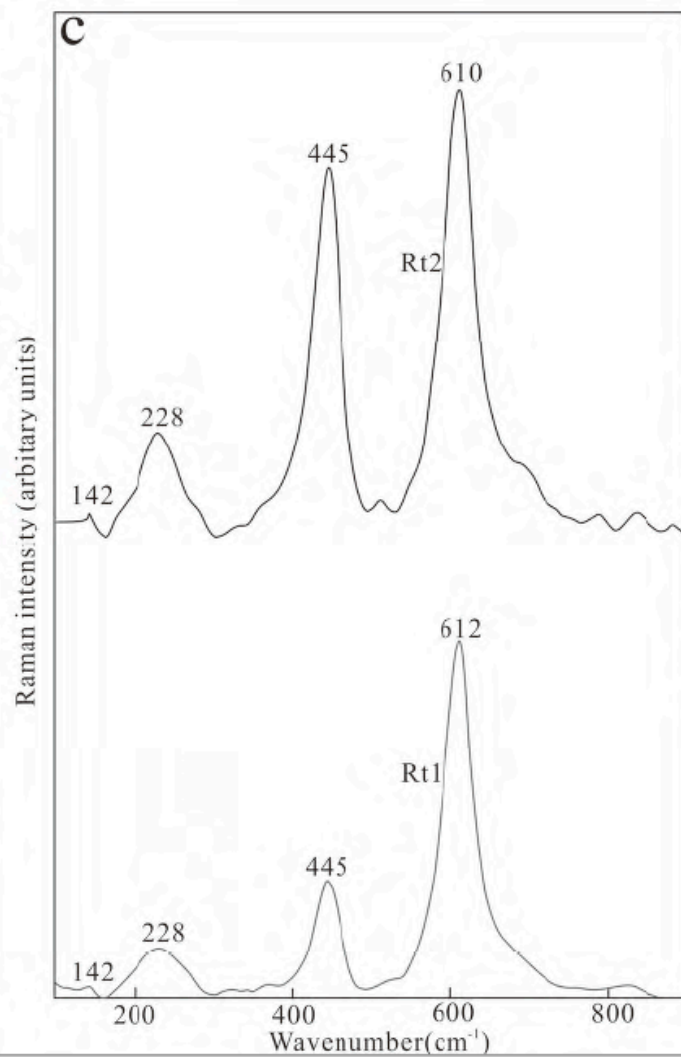
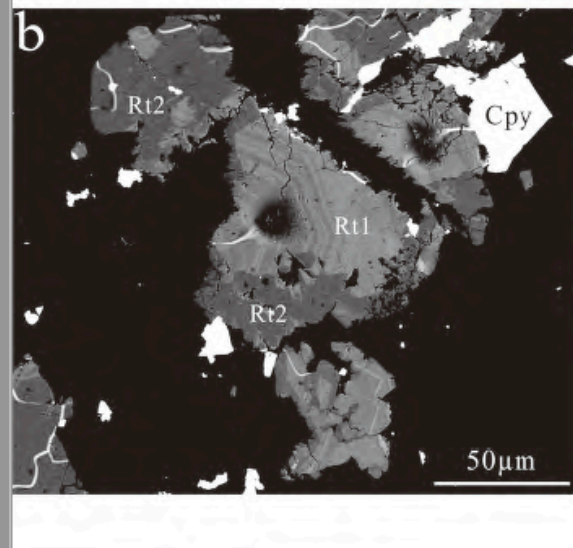
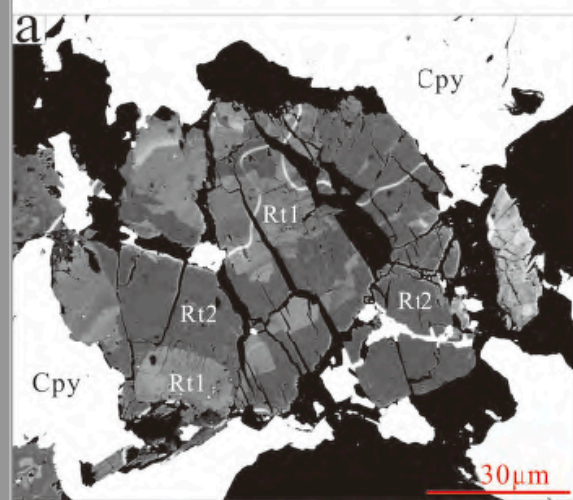


Figure 11

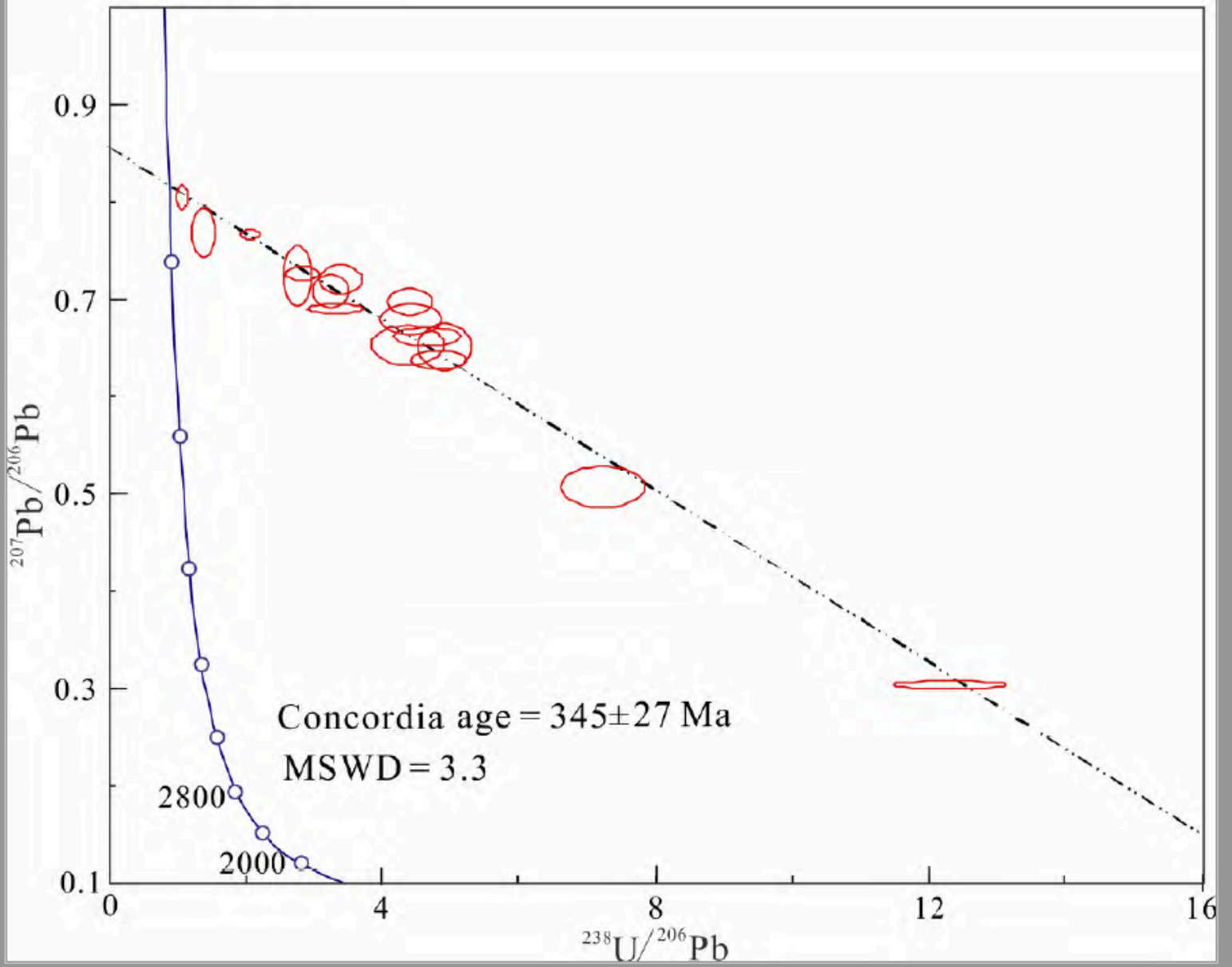


Figure 12

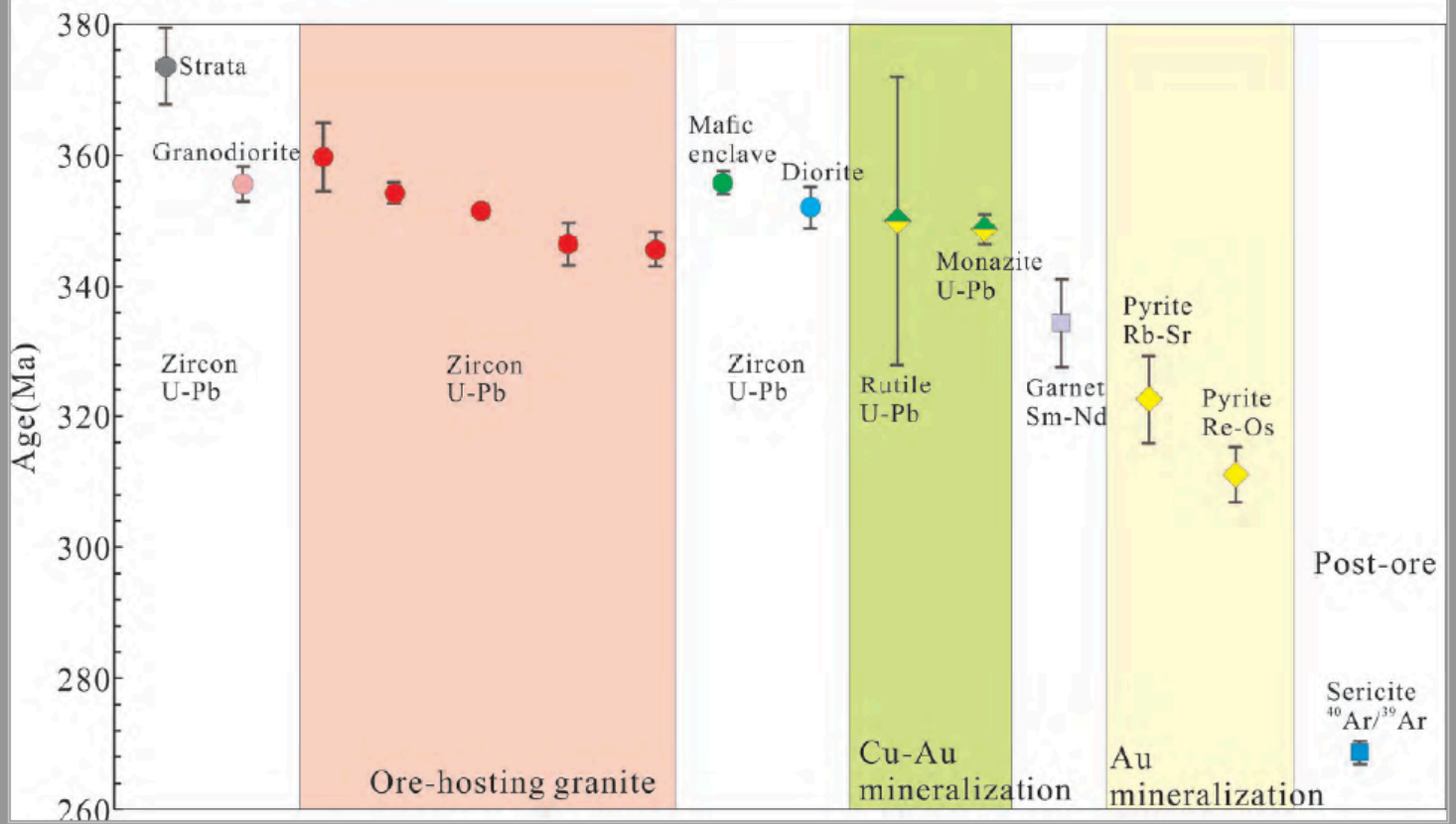


Table 1. Zircon SIMS U–Pb isotopic results for the Katbasu granite and mafic enclave

Sample@spot n	Elemental contents									
	U (ppm)	Th (ppm)	Th/U	$^{207}\text{Pb}/^{206}\text{Pb}$	1SE (%)	$^{207}\text{Pb}/^{235}\text{U}$	1SE (%)	$^{206}\text{Pb}/^{238}\text{U}$	1SE (%)	ρ^\dagger
Ore-hosted granite										
KT17-187-01	615	512	0.83	0.05362	0.70	0.41821	1.67	0.05657	1.51	0.91
KT17-187-02	1246	837	0.67	0.05426	0.52	0.42071	1.60	0.05624	1.52	0.95
KT17-187-03	738	484	0.66	0.05351	0.60	0.41537	1.63	0.05630	1.52	0.93
KT17-187-04	726	624	0.86	0.05331	0.69	0.41422	1.67	0.05635	1.53	0.91
KT17-187-05	221	164	0.74	0.05364	0.99	0.41439	1.80	0.05603	1.50	0.83
KT17-187-06	579	372	0.64	0.05339	1.16	0.41866	1.91	0.05687	1.51	0.79
KT17-187-07	720	791	1.10	0.05416	0.67	0.41288	1.69	0.05529	1.55	0.92
KT17-187-08	718	567	0.79	0.05327	0.63	0.41750	1.63	0.05684	1.50	0.92
KT17-187-09	701	397	0.57	0.05325	0.51	0.41616	1.59	0.05668	1.51	0.95
KT17-187-10	1300	1181	0.91	0.05411	0.39	0.42059	1.55	0.05637	1.51	0.97
Mafic enclave										
KT17-197-1	1307	1206	0.92	0.05359	0.51	0.41449	1.59	0.05609	1.51	0.95
KT17-197-2	1773	3187	1.80	0.05372	0.37	0.42418	1.55	0.05727	1.50	0.97
KT17-197-3	1235	2078	1.68	0.05396	0.60	0.42855	1.62	0.05760	1.51	0.93
KT17-197-4	2373	4583	1.93	0.05412	0.62	0.42951	1.62	0.05755	1.50	0.92
KT17-197-5	1656	3068	1.85	0.05385	1.82	0.42926	2.35	0.05781	1.50	0.64
KT17-197-6	2841	9160	3.22	0.05347	0.43	0.42658	1.59	0.05786	1.53	0.96
KT17-197-7	770	964	1.25	0.05347	1.15	0.40331	1.89	0.05470	1.50	0.79
KT17-197-8	764	827	1.08	0.05421	0.98	0.40970	1.81	0.05482	1.52	0.84

[†] ρ denotes error correlation between $^{207}\text{Pb}/^{235}\text{U}$ and $^{206}\text{Pb}/^{238}\text{U}$.

[§]Discordance is defined here as percent deviation of $t_{206/238}$ relative to $t_{207/206}$.

!.

$t_{207/206}$ (Ma)	1SE	$t_{207/235}$ (Ma)	1SE	$t_{206/238}$ (Ma)	1SE	cordance ^s (%)
355.1	15.8	354.8	5.0	354.7	5.2	-0.1
381.8	11.7	356.6	4.8	352.7	5.2	-7.8
350.3	13.5	352.7	4.9	353.1	5.2	0.8
342.1	15.6	351.9	5.0	353.4	5.2	3.4
356.0	22.2	352.0	5.4	351.4	5.1	-1.3
345.5	26.0	355.1	5.7	356.6	5.2	3.3
377.6	15.0	350.9	5.0	346.9	5.2	-8.4
340.4	14.2	354.3	4.9	356.4	5.2	4.8
339.6	11.4	353.3	4.8	355.4	5.2	4.8
375.8	8.7	356.5	4.7	353.5	5.2	-6.1
354.0	11.5	352.1	4.7	351.8	5.2	-0.6
359.3	8.4	359.0	4.7	359.0	5.2	-0.1
369.5	13.4	362.1	5.0	361.0	5.3	-2.4
376.2	14.0	362.8	5.0	360.7	5.3	-4.2
364.9	40.4	362.7	7.2	362.3	5.3	-0.7
348.9	9.8	360.7	4.8	362.6	5.4	4.0
348.9	25.7	344.0	5.5	343.3	5.0	-1.7
379.7	21.8	348.7	5.4	344.0	5.1	-9.7

Table 2. Results of LA-MC-ICP MS zircon U-Pb dating of diorite in the Katbasu Au-Cu deposit.

Spot	Sample number	Th	U	Th/U	$^{207}\text{Pb}^*/^{206}\text{Pb}^*$		$^{207}\text{Pb}^*/^{235}\text{U}$		$^{206}\text{Pb}^*/^{238}\text{U}$		$^{207}\text{Pb}/^{206}\text{Pb}$ (Ma)		$^{207}\text{Pb}/^{235}\text{U}$ (Ma)		$^{206}\text{Pb}/^{238}\text{U}$ (Ma)	
		($\times 10^{-6}$)			Ratio	1 σ	Ratio	1 σ	Ratio	1 σ	Age	1 σ	Age	1 σ	Age	1 σ
1	KT17-9-01	361	499	0.72	0.0579	0.0020	0.4636	0.0158	0.0577	0.0007	527.8	77.8	386.8	11.0	361.9	4.5
2	KT17-9-02	128	214	0.60	0.0571	0.0031	0.4728	0.0223	0.0604	0.0010	494.5	118.5	393.1	15.4	378.2	5.8
3	KT17-9-03	263	476	0.55	0.0548	0.0018	0.4392	0.0144	0.0579	0.0006	405.6	75.9	369.7	10.1	362.9	3.8
4	KT17-9-04	224	531	0.42	0.0600	0.0018	0.4951	0.0138	0.0598	0.0006	605.6	97.2	408.4	9.4	374.5	3.9
5	KT17-9-05	197	342	0.58	0.0572	0.0020	0.4766	0.0170	0.0602	0.0007	498.2	77.8	395.7	11.7	377.0	4.2
6	KT17-9-06	682	1015	0.67	0.0554	0.0014	0.4536	0.0111	0.0591	0.0005	427.8	55.6	379.8	7.8	370.1	3.2
7	KT17-9-07	279	426	0.66	0.0582	0.0019	0.5174	0.0167	0.0642	0.0008	600.0	70.4	423.4	11.2	401.2	4.7
8	KT17-9-08	378	1334	0.28	0.0590	0.0013	0.4964	0.0116	0.0608	0.0008	564.9	48.1	409.3	7.9	380.2	4.6
9	KT17-9-09	151	299	0.50	0.0555	0.0019	0.4536	0.0147	0.0591	0.0006	435.2	69.4	379.8	10.3	370.3	3.7
10	KT17-9-10	125	2731	0.05	0.0531	0.0012	0.4600	0.0113	0.0625	0.0008	331.5	53.7	384.2	7.9	391.1	4.6
11	KT17-9-11	243	398	0.61	0.0548	0.0016	0.4574	0.0136	0.0605	0.0007	466.7	66.7	382.5	9.4	378.4	4.4
12	KT17-9-12	1421	1310	1.08	0.0565	0.0014	0.4555	0.0110	0.0583	0.0006	472.3	53.7	381.2	7.6	365.1	3.7
13	KT17-9-13	473	553	0.86	0.0585	0.0023	0.4749	0.0157	0.0583	0.0006	550.0	85.2	394.5	10.8	365.1	3.7
14	KT17-9-14	1345	1935	0.70	0.0522	0.0012	0.4365	0.0106	0.0604	0.0007	300.1	55.6	367.8	7.5	378.1	4.1
15	KT17-9-15	5377	5521	0.97	0.0531	0.0011	0.4163	0.0083	0.0565	0.0005	331.5	44.4	353.4	6.0	354.3	3.1
16	KT17-9-16	384	464	0.83	0.0599	0.0029	0.4585	0.0165	0.0557	0.0005	611.1	100.9	383.2	11.5	349.4	3.2
17	KT17-9-17	389	596	0.65	0.0547	0.0017	0.4253	0.0123	0.0564	0.0006	398.2	75.0	359.8	8.7	353.6	3.4
18	KT17-9-18	393	555	0.71	0.0495	0.0033	0.3764	0.0247	0.0559	0.0006	172.3	157.4	324.4	18.2	350.6	3.6

Table 3. Results of LA-MC-ICP MS U-Pb dating of hydrothermal monazites in the Katbasu Au-Cu deposit.

Spot	Sample number	Pb	Th	U	Th/U	²⁰⁷ Pb/ ²⁰⁶ Pb		²⁰⁸ Pb/ ²³² Th		²⁰⁶ Pb*/ ²³⁸ U		²⁰⁷ Pb/ ²⁰⁶ Pb (Ma)		²⁰⁸ Pb/ ²³² Th (Ma)		²⁰⁶ Pb/ ²³⁸ U (Ma)	
		(×10 ⁻⁶)				Ratio	1σ	Ratio	1σ	Ratio	1σ	Age	1σ	Age	1σ	Age	1σ
1	KT17-41-1	42	1086	489	2.2	0.0545	0.0038	0.0155	0.0003	0.0566	0.0010	390.8	152.8	311.0	6.0	355.2	5.9
2	KT17-41-2	56	715	910	0.8	0.0529	0.0029	0.0164	0.0005	0.0550	0.0008	324.1	124.1	329.3	10.4	345.3	5.1
3	KT17-41-3	57	1091	789	1.4	0.0532	0.0029	0.0156	0.0003	0.0567	0.0007	344.5	122.2	313.3	5.6	355.4	4.1
4	KT17-41-4	49	1382	539	2.6	0.0602	0.0038	0.0160	0.0003	0.0548	0.0010	613.0	132.4	321.0	5.9	344.0	6.0
5	KT17-41-5	57	1726	625	2.8	0.0501	0.0029	0.0152	0.0002	0.0552	0.0009	198.2	137.0	305.2	4.6	346.6	5.3
6	KT17-41-6	83	855	1339	0.6	0.0537	0.0022	0.0165	0.0003	0.0550	0.0006	366.7	92.6	330.2	6.9	345.2	3.5
7	KT17-41-7	65	2314	598	3.9	0.0522	0.0035	0.0153	0.0002	0.0554	0.0008	294.5	153.7	307.5	4.2	347.8	5.0
8	KT17-41-8	56	2127	471	4.5	0.0555	0.0041	0.0164	0.0003	0.0570	0.0009	435.2	164.8	328.2	5.7	357.1	5.5
9	KT17-41-9	66	1622	816	2.0	0.0529	0.0027	0.0152	0.0002	0.0552	0.0008	324.1	112.0	305.5	4.5	346.2	4.6
10	KT17-41-10	45	930	601	1.5	0.0529	0.0031	0.0160	0.0004	0.0554	0.0008	324.1	131.5	320.2	7.1	347.4	4.9
11	KT17-41-11	61	520	1033	0.5	0.0506	0.0024	0.0158	0.0005	0.0546	0.0007	233.4	109.2	316.6	9.2	343.0	4.3
12	KT17-41-12	71	494	1229	0.4	0.0493	0.0021	0.0151	0.0004	0.0551	0.0007	166.8	100.0	303.0	8.6	345.7	4.1
13	KT17-41-13	86	624	1494	0.4	0.0535	0.0021	0.0161	0.0004	0.0544	0.0006	350.1	88.9	322.2	8.1	341.8	3.7
14	KT17-41-14	50	1156	643	1.8	0.0504	0.0029	0.0170	0.0003	0.0568	0.0008	213.0	133.3	340.0	6.7	356.4	4.8
15	KT17-41-15	35	1090	379	2.9	0.0560	0.0039	0.0178	0.0004	0.0558	0.0011	453.8	155.5	355.7	8.5	350.0	6.7
16	KT17-41-16	43	1589	414	3.8	0.0562	0.0048	0.0164	0.0003	0.0564	0.0012	461.2	189.6	328.1	6.2	353.9	7.4
17	KT17-41-17	53	821	792	1.0	0.0589	0.0029	0.0173	0.0005	0.0560	0.0007	561.1	105.5	345.7	9.1	351.3	4.2
18	KT17-41-18	55	1098	762	1.4	0.0575	0.0029	0.0169	0.0003	0.0549	0.0008	509.3	109.2	339.1	6.8	344.8	5.0
19	KT17-41-19	83	780	1425	0.5	0.0509	0.0020	0.0166	0.0004	0.0542	0.0006	239.0	88.9	333.1	8.3	340.0	3.7
20	KT17-41-20	53	1199	705	1.7	0.0525	0.0026	0.0170	0.0003	0.0565	0.0007	305.6	114.8	340.6	6.5	354.5	4.3
21	KT17-41-21	67	2440	672	3.6	0.0506	0.0029	0.0161	0.0002	0.0566	0.0009	233.4	133.3	322.5	4.2	354.9	5.4
22	KT17-41-22	30	659	410	1.6	0.0528	0.0040	0.0167	0.0004	0.0570	0.0009	320.4	141.7	334.7	7.7	357.3	5.4

23	KT17-41-23	52	2790	308	9.1	0.0554	0.0044	0.0173	0.0003	0.0567	0.0011	431.5	177.8	347.6	6.0	355.8	6.7
24	KT17-41-24	68	741	1151	0.6	0.0565	0.0026	0.0160	0.0004	0.0561	0.0008	472.3	100.0	321.0	8.2	352.0	4.8
25	KT17-41-25	66	2687	582	4.6	0.0532	0.0030	0.0165	0.0002	0.0571	0.0007	338.9	127.8	331.3	4.4	357.9	4.6
26	KT17-41-26	74	758	1310	0.6	0.0528	0.0024	0.0162	0.0004	0.0542	0.0006	316.7	105.5	325.6	7.8	340.5	3.9
27	KT17-41-27	66	1116	1012	1.1	0.0523	0.0026	0.0158	0.0004	0.0561	0.0008	298.2	108.3	316.4	7.0	351.8	4.7

Table 4. Results of SIMS U-Pb dating of W-rich rutile in the Katbasu Au-Cu deposit.

Sample	U (ppm)	Th (ppm)	Th/U	$^{238}\text{U}/^{206}\text{Pb}^{\#}$	$\pm 1\sigma$ (%)	$^{207}\text{Pb}/^{206}\text{Pb}^{\#}$	$\pm 1\sigma$ (%)	$f^{206\dagger}$	$t_{206/238}^*$ (Ma)	$\pm 1\sigma$ (%)
KT17-40-1	172	118	0.68	12.3224	2.74	0.3036	0.59	40.5	346.4	10.5
KT17-40-2	47	80	1.71	7.2299	3.51	0.5068	1.68	70.6	364.5	21.8
KT17-40-3	80	122	1.52	4.8328	3.44	0.6369	0.57	81.7	330.2	17.1
KT17-40-4	6	6	0.98	4.9332	3.20	0.6502	1.55	81.7	302.2	25.7
KT17-40-5	15	34	2.25	4.3820	4.89	0.6521	1.31	88.2	336.1	31.5
KT17-40-6	81	43	0.53	4.6627	4.34	0.6611	0.66	80.2	300.8	20.3
KT17-40-7	20	83	4.13	4.4222	4.21	0.6795	0.97	98.8	284.1	23.6
KT17-40-8	34	51	1.53	3.3209	5.11	0.6905	0.29	90.9	350.4	22.4
KT17-40-9	14	49	3.49	3.2505	3.30	0.7081	1.01	96.6	315.2	27.7
KT17-40-10	6	23	3.66	3.3929	3.82	0.7197	0.87	98.5	275.0	25.1
KT17-40-11	31	134	4.33	2.7836	2.98	0.7241	1.75	96.9	321.8	45.5
KT17-40-12	17	69	3.97	2.8436	3.66	0.7262	0.37	98.3	309.3	18.7
KT17-40-13	39	164	4.24	2.0561	2.83	0.7664	0.27	99.6	271.1	15.6
KT17-40-14	8	24	2.90	1.3853	4.86	0.7683	1.32	96.9	388.8	76.1
KT17-40-15	11	94	8.33	1.0668	3.61	0.8045	0.65	106.6	235.4	47.6
KT17-40-16	24	64	2.70	4.3994	3.06	0.6974	0.86	100.5	253.3	18.5

[#] The ratios are common Pb uncorrected, used for Tera–Wasserburg plot.

[†] f^{206} is the percentage of common ^{206}Pb in total ^{206}Pb , calculated by ^{207}Pb -based.

^{*} $t_{206/238}$ is ^{206}Pb – ^{238}U age calculated by ^{207}Pb -based common-lead correction.